Journal of Sound and Vibration 548 (2023) 117532

Contents lists available at ScienceDirect

Journal of Sound and Vibration

journal homepage: www.elsevier.com/locate/jsvi

Noise predictions of a Mach 0.9 round jet using tailored adjoint Green's functions

Étienne Spieser *, Christophe Bogey, Christophe Bailly

Laboratoire de Mécanique des Fluides et d'Acoustique (UMR 5509), Université de Lyon, CNRS, École Centrale de Lyon, Institut National des Sciences Appliquées de Lyon, Université Claude Bernard Lyon I, 69130 Écully, France

ARTICLE INFO

Keywords:
Jet noise
Sound propagation
Adjoint method
Tones

ABSTRACT

The turbulent mixing noise radiated by a Mach 0.9 jet is investigated. The focus is put on the proper calculation of acoustic propagation effects by means of adjoint Green's function that are tailored to the jet mean flow. Tam and Auriault's statistical mixing noise model is recast for Pierce's wave equation that is energy preserving. An unconditionally stable formulation to compute propagation effects is thus obtained. Adjoint fields are computed from the direct problem with help of the flow reversal theorem. A finite element solver is used to solve tailored adjoint Green's functions, and corresponding adjoint fields are displayed. Acoustic predictions are carried out for a wide range of polar angles, and compared to measurements. A particular attention is given to predictions achieved at upstream observer angles. At these angles, the present model describes the physics of upstream travelling guided jet waves. The adjoint method provides a suitable framework to split the generation of sound from its propagation. It is illustrated how tailored adjoint Green's functions filter the radiating part of Tam and Auriault's sound source model, by weighting with propagation effects.

1. Introduction

The modelling of turbulent mixing noise involves the expression of the noise spectrum S_{pp}. This quantity is of interest in many applications dealing with subsonic jet noise, including acoustic certification of aircraft [1]. For a microphone located at $\mathbf{x}_m$, the spectrum is obtained by considering the Fourier transform of the pressure autocorrelation defined in Appendix A,

$$S_{pp}(\mathbf{x}_m,\omega)=\int_{\mathbb{R}}\mathrm{d}\tau\ \ \overline{p(\mathbf{x}_m,\bullet)p(\mathbf{x}_m,\bullet+\tau)}e^{\mathrm{i}\,\omega\tau} \tag{1}$$

where ω denotes the angular frequency, where $\bullet$ stands for a dummy time variable, and where a stationary noise generation mechanism is assumed. Let us introduce Green's function $G^{(\mathbf{x}_m,t_m)}_{\mathbf{x}_s,t_s}$ to realise sound propagation from the source region Ω to the microphone one,

$$p(\mathbf{x}_m,t_m)=\int_{\mathbb{R}}\mathrm{d}t_s\int_{\Omega}\mathrm{d}\mathbf{x}_s\ \ G^{(\mathbf{x}_m,t_m)}_{\mathbf{x}_s,t_s}q(\mathbf{x}_s,t_s) \tag{2}$$

where $(\mathbf{x}_m,t_m)$ and $(\mathbf{x}_s,t_s)$ are associated with the observer and a current source in Ω respectively, and where q is the source term. The propagation problem is moreover time-shift invariant, $G^{(\mathbf{x}_m,t_m)}_{\mathbf{x}_s,t_s}=G^{(\mathbf{x}_m,t_m-t_s)}_{\mathbf{x}_s}$ for a steady base flow.

* Corresponding author.
E-mail address: etienne.spieser@ec-lyon.fr (É. Spieser).

https://doi.org/10.1016/j.jsv.2022.117532
Received 14 February 2022; Received in revised form 19 December 2022; Accepted 19 December 2022
Available online 23 December 2022

Acoustic analogies are often used in this context to reduce the computational cost, Lighthill's acoustic analogy [2] being the first and most famous formulation. In these approaches where the sound propagation is explicitly separated from generation, the spectrum S_{pp} is expressed from the two-point correlation R_{qq} of the source term,

$$S_{pp}(\mathbf{x}_m,\omega)=\int_{\mathbb{R}}\mathrm{d}\tau\int_{\mathbb{R}}\mathrm{d}t_1\int_{\mathbb{R}}\mathrm{d}t_2\int_{\Omega}\mathrm{d}\mathbf{x}_1\int_{\Omega}\mathrm{d}\mathbf{x}_2\;\; G_{\mathbf{x}_1}^{(\mathbf{x}_m,t_1)}G_{\mathbf{x}_2}^{(\mathbf{x}_m,t_2+\tau)}R_{qq}(\mathbf{x}_1,\mathbf{x}_2,t_1-t_2)e^{\mathrm{i}\,\omega\tau} \tag{3}$$

In the past, most of the efforts of improvements have focused in finding a proper description of the source correlation term R_{qq} by modelling the sound stemming from fluid dilatation [3,4], from the quadrupole correlations arising in isotropic turbulence [5–7] or those from more complex shell models of turbulence [8–10]. The definition of the source term q and its associated wave equation is also a critical step [11–13]. These modellings are however not so often used in practice because the numerical determination of Green's function $G_{\mathbf{x}_1}$ and $G_{\mathbf{x}_2}$ for all positions $\mathbf{x}_1$, $\mathbf{x}_2$ in the source domain Ω is not affordable.

Lagrange's identity [14,15] provides an especially suitable framework to shape further statistical models in giving a better account of sound propagation. By using the reciprocity principle in its most general form that involves adjoints, Green's functions for the acoustic propagation can be recast to depend solely on the receiver [15,16],

$$G_{\mathbf{x}_s,t_s}^{(\mathbf{x}_m,t_m)}=G^{\dagger\,(\mathbf{x}_s,t_s)}_{\mathbf{x}_m,t_m} \tag{4}$$

where $G^{\dagger}_{\mathbf{x}_m,t_m}$ is adjoint Green's function expressed for the microphone position $\mathbf{x}_m$ and time t_m, and for which a tacit choice of a suitable scalar product is made.

The first reformulation of Lighthill's acoustic analogy in the adjoint framework was proposed by Dowling et al. [16]. A major contribution was made by Tam and Auriault [4,17] for statistical jet noise modelling. Goldstein and Leib [18–20], Raizada and Morris [21] amongst other, proposed additional statistical jet noise models involving adjoints later on.

Statistical jet noise modelling has benefitted from the advances in computational science in providing an access to an accurate description of the source term's correlation R_{qq} [22–24] and in informing on the manner flow structures radiate to the observer [25–27]. Solving numerically adjoint Green's functions for arbitrary base flows and geometries has remained a challenge, and beside contributions done in the group of Karabasov [28,29], only adjoint Green's function tailored to some specific flow profiles have been used to account for the sound propagation in statistical models. In that case, adjoint Green's functions are often not known analytically, but their governing equations are smartly rearranged so to be tractable by ordinary differential equations. Sound is then considered to propagate either in the free field [30,31], over a plug flow [16], over a general parallel jet flow [17,21,32] or over a slowly diverging jet flow [18,33–36].

Spieser and Bailly [15] recently proposed the use of Pierce's wave equation to compute sound propagation in the adjoint framework. The self-adjoint nature of this operator possesses two main advantages, it guaranties the stability of the sound propagation problem and enables the computation of the adjoints with help of the handy flow reversal theorem. This study intends to evaluate numerically such adjoint Green's functions using a finite element solver, and aims to illustrate how the modelling and the understanding of jet noise can thereby be improved. Tam et al. [37,38] already highlighted on an experimental campaign how the adjoint formalism could be used to characterise and extrapolate the radiating parts of the coherent structures in jets. As explained in their study, the whole sound source is not contributing to the acoustic radiation, in fact, only the part filtered by the wave operator is. Green's functions are the formal inverse of an operator and adjoint Green's functions are therefore the appropriate tool to isolate the radiating parts of a sound source. On the basis of this observation, this contribution also means to illustrate how insight into the radiating parts of a jet can be gained within the adjoint framework.

The paper is organised as follows. Tam and Auriault's mixing noise model is reformulated for Pierce's wave equation in Section 2. The numerical procedure to compute tailored adjoint Green's functions in an efficient way is explained in Section 3. Mixing noise radiated in the sideline direction by a subsonic round jet at Mach 0.9 is investigated in Section 4. Section 5 is focused on the acoustic field radiated in the upstream direction and the emergence of tones. The influence of the nozzle for the computation of the acoustic field is discussed, and predictions for a wide range of polar angles are presented in Section 6. Concluding remarks are finally drawn in the last section. Calculation details have been included in the Appendices for ease of reading.

2. Jet mixing noise model for Pierce's wave equation

Tam et al. [39] gave experimental evidences for two contributions arising in the turbulent mixing noise process of a jet. The first one is associated with the large-scales of turbulence, often associated with the development of convective instability waves, while the second one originates from the turbulence fine scale. Shortly after, Tam and Auriault [4] proposed a statistical model to predict the noise spectra radiated by the latter component. The concern of this section is to reformulate their model for Pierce's wave equation.

2.1. Prequel of Tam and Auriault's model

The starting point for this model is based on an acoustic analogy, where the sound generation process and its propagation over a base flow are addressed separately. A parallel and steady base flow is assumed and forced linearised Euler's equation reads as,

$$\begin{cases}\rho_0\dfrac{\mathrm{D}(\mathbf{u})}{\mathrm{D}t}+\nabla p=-\nabla\cdot(\rho_0\mathbf{u}\otimes\mathbf{u})\\[2ex]\dfrac{\mathrm{D}(p)}{\mathrm{D}t}+\gamma p_0(\nabla\cdot\mathbf{u})=0\end{cases} \tag{5}$$

where $\mathrm{D}/\mathrm{D}t = \partial/\partial t + \mathbf{u}_0 \cdot \nabla$ is the material derivative along the mean flow. The fluctuating variables are written without subscript nor superscript, and the mean flow field is indexed with $_0$. The non linear source term on the right-hand side of the momentum equation has been identified by Bogey et al. [40] and discussed later [41]. As also underlined in these previous studies, Pierce's wave equation does not describe instability waves [15] and is therefore particularly well suited to be used in an acoustic analogy. Introducing the acoustic potential ϕ as $p = -\mathrm{D}(\phi)/\mathrm{D}t$, and a_0 the speed of sound, an acoustic analogy based on Pierce's equation can be derived [15,42],

$$\frac{\mathrm{D}^2(\phi)}{\mathrm{D}t^2} - \nabla \cdot (a_0^2 \nabla \phi) = \frac{\mathrm{D}(S_m)}{\mathrm{D}t}\,, \qquad \nabla^2 S_m = \nabla \cdot \nabla \cdot (\rho_0 \mathbf{u} \otimes \mathbf{u}) \tag{6}$$

where the source term presented in Eq. (6) has been reduced to its main contribution provided by Reynolds stress tensor. A drastic simplification of the source term is considered in Tam and Auriault [4] by contracting the instantaneous Reynolds stress tensor $\rho_0\ \mathbf{u}\ \otimes\ \mathbf{u} \approx q_s\ \mathbf{I}$, where q_s is linked to the turbulent kinetic energy and $\mathbf{I}$ is the identity matrix. As a result, the source term in Eq. (5) is reduced to,

$$-\nabla \cdot \left(\rho_0 \mathbf{u} \otimes \mathbf{u}\right) \approx -\nabla q_s \tag{7}$$

and its quadrupolar feature is lost. Identification with the acoustic analogy built for Pierce's wave equation (6) is straightforward and leads to,

$$S_m = -q_s \tag{8}$$

2.2. Recast of the model

2.2.1. Adjoint statement of the problem

Pierce's wave equation (6) is self-adjoint for the canonical scalar product defined in Appendix A, and its adjoint Green's function $\phi^\dagger_{\mathbf{x}_m,t_m}$ is the anti-causal solution of,

$$\frac{\mathrm{D}^2(\phi^\dagger_{\mathbf{x}_m,t_m})}{\mathrm{D}t^2} - \nabla \cdot (a_0^2 \nabla \phi^\dagger_{\mathbf{x}_m,t_m}) = \delta_{\mathbf{x}_m,t_m} \tag{9}$$

where $\delta_{\mathbf{x}_m,t_m}$ is the Dirac delta function taken at the microphone position $\mathbf{x}_m$ and time t_m. Applying Lagrange's identity [15, Eq. (4.4)] with adjoint Green's function $\phi^\dagger_{\mathbf{x}_m,t_m}$ then directly leads to,

$$\phi(\mathbf{x}_m, t_m) = \langle \phi^\dagger_{\mathbf{x}_m,t_m}, -\frac{\mathrm{D}(q_s)}{\mathrm{D}t} \rangle \tag{10}$$

2.2.2. Calculation of the acoustic noise spectra

Choosing Pierce's wave equation to describe the propagation of sound, the acoustic spectral density S_{pp} in Eq. (1) can then be recast as,

$$S_{pp}(\mathbf{x}_m, \omega) = \int_{\mathbb{R}} \mathrm{d}\tau \overline{\frac{\mathrm{D}(\phi)}{\mathrm{D}_{\bullet,\mathbf{x}_m}} \frac{\mathrm{D}(\phi)}{\mathrm{D}_{\bullet+\tau,\mathbf{x}_m}}} e^{\mathrm{i}\omega\tau} \tag{11}$$

where $\mathrm{D}/\mathrm{D}_{t_A,\mathbf{x}_B} = \partial/\partial t_A + \mathbf{u}_0 \cdot \partial/\partial \mathbf{x}_B$ is the material derivative with respect to the position $\mathbf{x}_B$ and the reference time t_A. This cumbersome notation is used in the following whenever there may be a confusion in the variables on which the material derivative applies and is omitted elsewhere. Following the derivations provided in Appendix B, expressing previous relationship with help of adjoint Green's functions, leads to,

$$S_{pp}(\mathbf{x}_m, \omega) = \int_{\mathbb{R}} \mathrm{d}\tau \int_\Omega \mathrm{d}\mathbf{x}_1 \int_\Omega \mathrm{d}\mathbf{x}_2 \int_{\mathbb{R}} \mathrm{d}\tilde{t}_1 \int_{\mathbb{R}} \mathrm{d}\tilde{t}_2 \ \frac{\mathrm{D}\left(\phi^{\dagger(\mathbf{x}_1,\tilde{t}_1)}_{\mathbf{x}_m}\right)}{\mathrm{D}_{-\tilde{t}_1,\mathbf{x}_m}} \frac{\mathrm{D}\left(\phi^{\dagger(\mathbf{x}_2,\tilde{t}_2-\tau)}_{\mathbf{x}_m}\right)}{\mathrm{D}_{-\tilde{t}_2,\mathbf{x}_m}} R_{QQ}(\mathbf{x}_1, \mathbf{x}_2, \tilde{\tau}) e^{\mathrm{i}\omega\tau} \tag{12}$$

where $\tilde{\tau} = \tilde{t}_1 - \tilde{t}_2$ is the time separation and R_{QQ} is the space–time correlation defined as,

$$R_{QQ}(\mathbf{x}_1, \mathbf{x}_2, \tilde{\tau}) \equiv \overline{\frac{\mathrm{D}(q_s(\mathbf{x}_1, \bullet + \tilde{\tau}))}{\mathrm{D}_{\bullet,\mathbf{x}_1}} \frac{\mathrm{D}(q_s(\mathbf{x}_2, \bullet))}{\mathrm{D}_{\bullet,\mathbf{x}_2}}} \tag{13}$$

To compute the acoustic spectral density, only the time-shifts in the source correlation are of significance. Adjoint Green's functions and the material derivative that apply on them can thus be expressed in the frequency domain to obtain the concise form,

$$S_{pp}(\mathbf{x}_m, \omega) = \int_\Omega \mathrm{d}\mathbf{x}_1 \int_\Omega \mathrm{d}\mathbf{x}_2 \ \mathrm{D}_{-\mathbf{u}_0,\mathbf{x}_m}\left(\phi^{\dagger(\mathbf{x}_1,\omega)}_{\mathbf{x}_m}\right) \mathrm{D}_{-\mathbf{u}_0,\mathbf{x}_m}\left(\phi^{\dagger(\mathbf{x}_2,-\omega)}_{\mathbf{x}_m}\right) \int_{\mathbb{R}} \mathrm{d}\tilde{\tau} \ R_{QQ}(\mathbf{x}_1, \mathbf{x}_2, \tilde{\tau}) e^{-\mathrm{i}\omega\tilde{\tau}} \tag{14}$$

where the Fourier transform conventions introduced in Appendix A are chosen. Eq. (14) is the most advanced expression of the noise spectrum that can be derived from Eqs. (6) and (7) without introducing further hypothesis.

2.2.3. Far field approximation

In classical jet noise applications, Fraunhofer's far field condition is satisfied [43]. This approximation is made here to make the evaluation of the double volume integral over the source region more tractable. Introducing the separation vector $\mathbf{r} = \mathbf{x}_1 - \mathbf{x}_2$ between two points $\mathbf{x}_1$ and $\mathbf{x}_2$ in the jet region, enables to link an acoustic ray reaching an observer position $\mathbf{x}_m$ to a neighbouring ray by modelling only the phase shift in between them. Following Tam and Auriault's work, two neighbouring acoustic ray paths are related by,

$$\phi^{\dagger(\mathbf{r}+\mathbf{x}_2,\omega)}_{\mathbf{x}_m} \approx \phi^{\dagger(\mathbf{x}_2,\omega)}_{\mathbf{x}_m} \exp\left(\frac{\mathrm{i}\,\omega\,\mathbf{x}_m\cdot\mathbf{r}}{a_\infty|\mathbf{x}_m|}\right) \tag{15}$$

where a_∞ is the ambient speed of sound. Replacing this formula in the expression of S_{pp}, and some calculus detailed again in Appendix B provide,

$$S_{pp}(\mathbf{x}_m,\omega) = \int_\Omega \mathrm{d}\mathbf{x}_s \left|\mathrm{D}_{-\mathbf{u}_0,\mathbf{x}_m}\left(\phi^{\dagger(\mathbf{x}_s,\omega)}_{\mathbf{x}_m}\right)\right|^2 \int_\Omega \mathrm{d}\mathbf{r}\int_{\mathbb{R}} \mathrm{d}\tilde{\tau}\;\; R_{QQ}(\mathbf{x}_s,\mathbf{r},\tilde{\tau})\, e^{\mathrm{i}\,\omega\left[\frac{\mathbf{x}_m\cdot\mathbf{r}}{a_\infty|\mathbf{x}_m|}-\tilde{\tau}\right]} \tag{16}$$

Please note that the use of this far-field approximation implies a simplification of the physics of the problem, as no phase differences are accounted for when $\mathbf{x}_m\cdot\mathbf{r} = 0$, according to Eq. (15). Depending on the expression of the source correlation term R_{QQ}, this approximation may thus entail a singularity for observer located in a direction normal to the jet axis. In particular, if at the leading order in $\mathbf{r}$, the expression of the source correlation behaves in $R_{QQ} \propto \exp\left(|\mathbf{r}|^\alpha\right)$, then it is becomes singular for an observer located normal to the jet axis when $\alpha \leq 1$. Future study may investigate the benefit of using a Taylor expansion to replace equation (15).

2.2.4. Modelling of the source correlation term R_{QQ}

In this study, the Q-quantity space–time correlation model used by Tam and Auriault [4, Eq. (27)][3, § III.] is considered,

$$R_{QQ}(\mathbf{x}_s,\mathbf{r},\tilde{\tau}) = \frac{\hat{q}_s^2}{\tau_s^2}\exp\left(-\frac{|\mathbf{r}\cdot\mathbf{u}_0|}{u_0^2\tau_s} - \frac{\ln(2)}{l_s^2}\left(\mathbf{r}-\tilde{\tau}\mathbf{u}_0\right)^2\right) \tag{17}$$

where $u_0 = |\mathbf{u}_0|$. In other words, turbulence is assumed to be locally homogeneous. The mean velocity $\mathbf{u}_0$ and the local quantities $\hat{q}_s$, τ_s and l_s measuring the turbulence intensity, decay time and correlation length, are informed by the statistics of the flow as provided for instance by a Reynolds-averaged Navier–Stokes flow solution. These three variables are function of the position $\mathbf{x}_s$ in the jet volume. This model for the source correlation R_{QQ} result in subsequent expression for the sound pressure level S_{pp}, details are provided in Appendix B,

$$S_{pp}(\mathbf{x}_m,\omega) = \int_\Omega \mathrm{d}\mathbf{x}_s \;\frac{2\hat{q}_s^2 l_s^3}{\tau_s}\left(\frac{\pi}{\ln(2)}\right)^{3/2}\left|\mathrm{D}_{-\mathbf{u}_0,\mathbf{x}_m}\left(\phi^{\dagger(\mathbf{x}_s,\omega)}_{\mathbf{x}_m}\right)\right|^2 \frac{\exp\left(\dfrac{-\omega^2 l_s^2}{4\ln(2)u_0^2}\left(1+\dfrac{u_0^2|\mathbf{x}_{m,\perp}|^2}{a_\infty^2|\mathbf{x}_m|^2}\right)\right)}{1+\omega^2\tau_s^2\left(1-\dfrac{\mathbf{u}_0\cdot\mathbf{x}_m}{a_\infty|\mathbf{x}_m|}\right)^2} \tag{18}$$

where $\mathbf{x}_{m,\perp} = \mathbf{x}_m - (\mathbf{x}_m\cdot\mathbf{u}_0)\mathbf{u}_0/u_0^2$, and where $\mathrm{D}_{-\mathbf{u}_0,\mathbf{x}_m}$ is the material derivative along $-\mathbf{u}_0$ taken at the position $\mathbf{x}_m$ and expressed in the frequency domain. This relation is comparable with the one proposed by Tam and Auriault [4, Eq. (35)], apart from original adjoint Green's function $p^{\dagger(\mathbf{x}_s,\omega)}_{\mathbf{x}_m}$ that is replaced by $\mathrm{D}_{-\mathbf{u}_0,\mathbf{x}_m}\left(\phi^{\dagger(\mathbf{x}_s,\omega)}_{\mathbf{x}_m}\right)$.

2.2.5. Final expression

The material derivative $\mathrm{D}_{-\mathbf{u}_0,\mathbf{x}_m}\left(\phi^{\dagger(\mathbf{x}_s,\omega)}_{\mathbf{x}_m}\right)$ can be expressed analytically in presence of flight effects, that is when the ambient media is moving at a constant velocity $\mathbf{u}_f$. The intermediate steps are reported in Appendix B. In the end, for a microphone located in the far-field at an angle θ_m from the jet axis, as illustrated in Fig. 3, Tam and Auriault's mixing noise formula can be recast for Pierce's wave equation into,

$$S_{pp}(\theta_m,\omega) = \int_\Omega \mathrm{d}\mathbf{x}_s \;\frac{2\omega^2\hat{q}_s^2 l_s^3}{\tau_s}\left(\frac{\pi}{\ln(2)}\right)^{3/2}\left|\phi^{\dagger(\mathbf{x}_s,\omega)}_{\theta_m}\right|^2\left(1+\frac{M_f\cos\theta_m}{1+M_f\cos\theta_m}\right)^2 \frac{\exp\left(\dfrac{-\omega^2 l_s^2}{4\ln(2)u_0^2}\left(1+M_\infty^2\sin^2\theta_m\right)\right)}{1+\omega^2\tau_s^2\left(1-M_\infty\cos\theta_m\right)^2} \tag{19}$$

where $M_\infty = u_0/a_\infty$ is the local acoustic Mach number and the flight Mach number is $M_f = |\mathbf{u}_f|/a_\infty$. The azimuthal dependency on the microphone position ψ_m is not accounted for, it is however fairly straightforward to include such effects in the derivations.

2.3. Calibration of the parameters

In the present analysis, the parameters $\hat{q}_s$, τ_s and l_s appearing in Eq. (19) are informed by a statistical description of the jet flow. This is often performed from a Reynolds-averaged Navier–Stokes solution. Here, the statistical results considered for the modelling are obtained from the large-eddy simulation (LES) of an isothermal jet at a Mach number of 0.9 and a Reynolds number based on the diameter D_J of $Re_{D_J} = 10^5$. The LES has been carried out using an in-house solver of the three-dimensional filtered compressible Navier–Stokes equations in cylindrical coordinates based on low-dissipation and low-dispersion explicit schemes using a grid containing approximately one billion points [44]. The jet originate at $z = 0$ from a straight pipe nozzle of radius $D_J/2$ and

length D_J, into a medium at rest at a temperature 293 K and a pressure 10^5 Pa. A Blasius laminar boundary-layer profile is imposed for the axial velocity at the pipe inlet at $z = -D_J$, yielding a momentum boundary-layer thickness of $0.009D_J$ at the exit. Random low-level vortical disturbances are also added inside the pipe [45,46] with a magnitude adjusted to obtain a peak turbulence intensity of 9% at the exit. During the simulation, density, velocity components and pressure have been recorded at several locations during a time of $T = 2\,000D_J/u_j$, creating a data base described in Ref. [47], for instance. More details and results of the jet LES can be found in previous studies [27,48,49].

In their contribution, Tam and Auriault proposed to model the parameters $\hat{q}_s$, τ_s and l_s from a $k-\varepsilon$ flow solution [4] considering following relationships,

$$l_s \propto \frac{k^{3/2}}{\varepsilon}\,, \qquad \tau_s \propto \frac{k}{\varepsilon} \quad \text{and,} \quad \hat{q}_s \propto \rho_0 k \tag{20}$$

so that only three constants were left to calibrate. In this work the number of independent variables is reduced to two by assuming that the characteristic time scale τ_s, which corresponds to the life time of turbulence, and length scale l_s of Tam and Auriault's model are related in a moving reference frame by u'_{ref} that is a measure of the turbulent velocity, such as,

$$\tau_s = \frac{l_s}{u'_{\text{ref}}}\,, \qquad \text{with,} \qquad u'_{\text{ref}} = \sqrt{\frac{2}{3}k_{\max}} \tag{21}$$

and, where $k_{\max} \equiv k_{\max}(z)$ is the maximum value of the turbulent kinetic energy k in a plane of constant z. From dimensional considerations, k [$\text{m}^2 \cdot \text{s}^{-2}$] and ε [$\text{m}^2 \cdot \text{s}^{-3}$] must then be linked by a characteristic time scale of the mean flow [50] [51, chap.9]. In the following, the turbulent dissipation rate ε is reconstructed from,

$$\varepsilon \propto k \left|\frac{\partial u_z}{\partial r}\right|_{\max} \tag{22}$$

where $|\partial u_z/\partial r|_{\max} \equiv |\partial u_z/\partial r|_{\max}(z)$ is the maximal shear in a plane of constant z. Finally from Eqs. (20) and (22), l_s can be expressed as,

$$l_s \propto \sqrt{k}/\left|\frac{\partial u_z}{\partial r}\right|_{\max} \tag{23}$$

Only the mean flow and turbulent kinetic energy k are consequently required to calibrate l_s and τ_s. This is expected to make the calibration procedure fairly independent from the flow solver.

It is now argued that l_s corresponds to an integral length scale of the turbulence computed in a direction transverse to the jet flow. Let us consider a given instant of the source such that $\tilde{\tau} = 0$, and let σ be the standard deviation associated to the Gaussian source correlation R_{QQ}, then $R_{QQ}(\mathbf{x}_s, \mathbf{r}, \tilde{\tau} = 0) = (\hat{q}_s^2/\tau_s^2)\exp\left(-\mathbf{r}^2/(2\sigma^2)\right)$. From the expression of R_{QQ} presented in Eq. (17), the source correlation can be expressed as $R_{QQ}(\mathbf{x}_s, \mathbf{r}, \tilde{\tau} = 0) = (\hat{q}_s^2/\tau_s^2)\exp\left(-\ln(2)\mathbf{r}^2/l_s^2\right)$, whenever $\mathbf{r}\cdot\mathbf{u}_0 = 0$. Thus for a separation vector transverse to the flow direction, $l_s = \sqrt{2\ln(2)}\sigma$ which is precisely the expression of the half width at the half maximum of a Gaussian distribution. To verify that this measure is equal to an integral length scale l_i, this latter length is computed in the transverse direction from the source correlation function given in Eq. (17),

$$l_i(\mathbf{x}_s) = \int_0^\infty \frac{R_{QQ}(\mathbf{x}_s, (0,\xi,0), 0)}{|R_{QQ}(\mathbf{x}_s, \mathbf{0}, 0)|}\mathrm{d}\xi = \int_0^\infty e^{-\frac{\ln(2)\xi^2}{l_s(\mathbf{x}_s)^2}}\mathrm{d}\xi = \frac{l_s(\mathbf{x}_s)}{2}\sqrt{\frac{\pi}{\ln(2)}} \approx 1.064\, l_s(\mathbf{x}_s) \tag{24}$$

It turns out that l_s corresponds to the transversal integral length scale of the Gaussian distribution R_{QQ} within 6%.

Without any direct access to the distribution of R_{QQ}, the latter distribution is assumed to be similar to that of $R_{u'_z u'_z}$. There are experimental [52] and theoretical [5,53] arguments indicating that turbulence in the plumes of jets can reasonably be assumed as homogeneous and isotropic. Within this assumption, if $L_{11}^{(1)}$ is the longitudinal integral length scale computed from $R_{u'_z u'_z}$ as defined in [52], then $l_s \approx L_{11}^{(1)}/2$. The longitudinal integral length scale $L_{11}^{(1)}$ has been computed along the jet lip-line from the large-eddy simulation [27], and serves as a reference for the calibration of Eq. (23). Two evaluations of formula (23) along the jet lipline are presented in Fig. 1 for which proportionality constants of 1.0 and 2.0 are used respectively. These transversal scales l_s are compared to the reference longitudinal length scale $L_{11}^{(1)}$. As expected, the size of the structures grow linearly with the axial distance z. The slope of l_s computed for a proportionality constant of 2.0 is comparable with that of $L_{11}^{(1)}$, indicating that l_s should be computed from Eq. (23) considering a proportionality constant equal to 1.0.

To calibrate the amplitude $\hat{q}_s$ of the source correlation defined in Eq. (20), the noise spectra radiated at $\theta_m = 90°$ from the axis of a Mach number 0.9 isothermal round jet is considered. Noise spectra are expressed in dB/St, they are normalised to a distance of 1 m and corrected so as to correspond to an equivalent jet of $1\,\text{m}^2$. The Fourier transform of the pressure autocorrelation S_{pp} obtained with Tam and Auriault's formula is hence related to the normalised sound pressure level (SPL) by,

$$\text{SPL(dB/St)} = 10\log_{10}\left(\frac{S_{pp}(\mathbf{x}_m, \omega)}{p_{\text{ref}}^2}\right) + 10\log_{10}\left(\frac{u_j}{D_J}\right) - 10\log_{10}\left(\frac{\pi D_J^2}{4}\right) + 10\log_{10}\left(|\mathbf{x}_m|^2\right) \tag{25}$$

where $p_{\text{ref}} = 20.0\,\mu\text{Pa}$ and $|\mathbf{x}_m|$ corresponds to the distance from the jet exhaust to the microphone position. The Strouhal number St is based on the jet diameter D_J and exhaust velocity u_j such that, $\text{St} = \omega D_J/(2\pi u_j)$. At $\theta_m = 90°$ from the jet axis, mean flow refraction effects are deemed not of leading order and without external wind, Green's function appearing in Tam and Auriault's formula may be approximated with,

$$\left|\mathrm{D}_{-\mathbf{u}_0,\mathbf{x}_m}(\phi^{\dagger(\mathbf{x},\omega)}_{\mathbf{x}_m})\right|^2 = \frac{\omega^2}{16\pi^2 a_0^4 |\mathbf{x}-\mathbf{x}_m|^2} \tag{26}$$

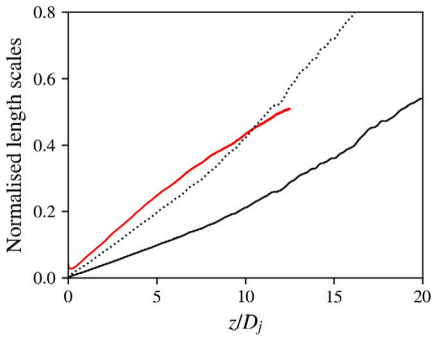

Fig. 1. Evolution of the longitudinal and transversal integral length scales $L_{11}^{(1)}$ and l_s along the jet lip-line normalised by the jet diameter D_J. —— reference $L_{11}^{(1)}/D_J$ directly calculated from the large-eddy flow solution for two points separated in the streamwise direction and compensated according to Eq. (24), —— l_s/D_J rebuilt from Eq. (23) considering a proportionality factor set to 1.0, and ····· l_s/D_J computed from Eq. (23) for a proportionality constant of 2.0.

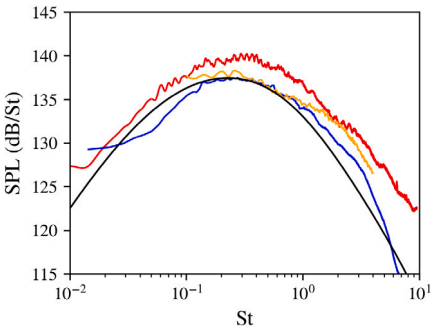

Fig. 2. Acoustic spectral density at $\theta_m = 90°$ from the axis of a Mach 0.9 round jet normalised to an equivalent distance of 1 m and to equivalent jet cross-section of 1 m^2. —— ECL data [49,55], —— CNRS-Pprime data [56,57], —— computed from the LES acoustic field extrapolated at a distance of 75 D_J from the jet axis [48,49,54], and, —— predictions of the mixing noise model with an amplitude calibration set to 1.0.

The derivation of this expression is provided in Appendix C. This analytical Green's function is used to evaluate the noise spectra model given in Eq. (18).

The acoustic spectra computed for $\hat{q}_s = \rho_0 k$, i.e. without fine-tuning of the amplitude of the source space–time correlation R_{QQ}, is plotted in Fig. 2. As previously l_s and τ_s are related through Eq. (21) and $l_s = \sqrt{k}/|\partial u_z/\partial r|_{\max}$ is considered. The thereby obtained noise spectra is compared in Fig. 2 to the spectral density computed from the LES of the Mach 0.9 round jet [48,49,54] that is used in this study to inform the sound source correlation R_{QQ}. This figure additionally displays two acoustic spectra measured at $\theta_m = 90°$ from two Mach 0.9 isothermal round jets, one during a ECL (École Centrale de Lyon) campaign [49,55], the other at CNRS-Pprime during the JERONIMO campaign [56,57]. A sensible prediction in terms of level, peak frequency and width of the jet noise hump is obtained in Fig. 2 for the recast of Tam and Auriault's mixing noise model presented in this study. This result is all the more satisfactory as no particular tuning of the sound source parameters has been used. Note how the crudely simple free field analytical solution given in Eq. (26) provides a fair prediction at $\theta_m = 90°$ from the jet axis [30,31]. While the acoustic levels computed from the LES and that recorded at CNRS-Pprime are closely recovered by the model, the jet investigated at ECL is 2.5 dB louder. This difference is significant, but is typical of the discrepancies that can be encountered between different acoustic test campaigns of jets presenting different nozzle-exit boundary layer states [58–60]. To enable far field acoustic measurements in directions that are upstream of the jet, the nozzle considered during the ECL test campaign has been extended by a straight conduit [55, Fig.1 & Fig.2] and its nozzle exit boundary layer profile differs thus from that of the two other jets. As a section of this study focusses on the acoustic field radiated upstream of the jet, noise spectra from the ECL campaign are considered in what follows.

3. Computation of tailored adjoint Green's functions with `Actran TM`

Choosing a self-adjoint operator such as Pierce's wave equation (6) to compute the radiation of sound has two major advantages. Along with ensuring the conservation of the acoustic energy, and thus preventing the development of instability waves, this feature enables the computation of adjoint solutions to Pierce's wave equation (9) by making use of the flow reversal theorem (FRT). The equivalence of both statements has recently been highlighted for self-adjoint operators [15]. The FRT is more handy to use than computing adjoints, since no anti-causal boundary conditions are required, only the mean-flow direction has to be reversed. This can fairly easily be achieved with some off-the-shelf solver. In this work, the frequency-domain commercial solver `Actran TM` is employed for that purpose.

3.1. Acoustic equation implemented in Actran TM

The finite element method solver chosen however does not solve Pierce's wave Eq. (6), but a linearised and normalised expression of Möhring's equation [12]. If B is the fluctuating total enthalpy, Actran TM then considers as dependent variable the normalised fluctuating stagnation enthalpy b, that is defined by,

$$\mathrm{d}b = \rho_{T,0}\mathrm{d}B \tag{27}$$

where $\rho_{T,0}$ is the mean total density,

$$\rho_{T,0} = \rho_0 \left(1 + \frac{\gamma-1}{2}\mathbf{M}_0^2\right)^{1/(\gamma-1)} \tag{28}$$

This variable is related to the acoustic pressure p through $\partial p/\partial t = (\rho_0/\rho_{T,0})\mathrm{D}b/\mathrm{D}t$, and Möhring's equation solved by Actran TM expresses then as,

$$\frac{\partial}{\partial t}\left[\frac{\rho_0}{\rho_{T,0}^2 a_0^2}\frac{\mathrm{D}b}{\mathrm{D}t}\right] + \nabla\cdot\left[\frac{\rho_0\mathbf{u}_0}{\rho_{T,0}^2 a_0^2}\frac{\mathrm{D}b}{\mathrm{D}t} - \frac{\rho_0}{\rho_{T,0}^2}\nabla b\right] = S \tag{29}$$

where S is a generic sound source.

3.2. Solving Pierce's wave equation with Actran TM

Pierce's wave equation (6) and Möhring's equation (29) are both scalar convected wave equations. Both equations are in fact related one with another by a change of variable, and it is possible in practice to solve Pierce's wave equation (6) with Actran TM by preprocessing the mean-flow fields specified in input. Let $\rho_{0,C}$, $p_{0,C}$, $\mathbf{u}_{0,C}$ and $a_{0,C}$ be the customised inputs that achieve this transformation and which enable to solve Pierce's wave equation for a mean-flow given by ρ_0, p_0, $\mathbf{u}_0$ and a_0. From a direct comparison between Eqs. (6) and (29), it follows,

$$\mathbf{u}_{0,C} = \mathbf{u}_0\ , \qquad a_{0,C} = a_0\ , \qquad \text{and} \qquad \frac{\rho_{0,C}}{\rho_{T,0}^2} = \frac{1}{\rho_0} \tag{30}$$

To verify these relationships, the mean flow must be preprocessed accordingly,

$$\frac{p_{0,C}}{p_0} = \frac{\rho_{0,C}}{\rho_0} = \left[1 + \frac{\gamma-1}{2}\frac{\mathbf{u}_0^2}{a_0^2}\right]^{-2/(\gamma-1)} \tag{31}$$

where it has been assumed that the mean pressure p_0 is constant. This is a very reasonable approximation for parallel flows such as jets.

This change of variable must additionally be reflected in the amplitude of the source term either prior to the computation or be compensated a posteriori in the acoustic field computed. Let b the solution obtained with the solver when an impulsive source of unitary amplitude is considered and the preprocessing describe in Eq. (31) applied. The acoustic solution must then be compensated to retrieve the correct solution of Pierce's wave equation, considering,

$$\phi = \frac{\mathrm{i}\,\omega}{4\pi a_{0,S}^2}\left(1 + \frac{\gamma-1}{2}\frac{\mathbf{u}_{0,S}^2}{a_{0,S}^2}\right)^{-1/(\gamma-1)} b^* \tag{32}$$

where b^* is the complex conjugate of b, ω the acoustic pulsation considered, $a_{0,S}$, and $\mathbf{u}_{0,S}$, the speed of sound and mean velocity evaluated at the source position. The source amplitude considered in Actran TM is defined with respect to the pressure (variable AMPLITUDE_TYPE set to P). Note that this correction holds for a three dimensional space, if a bidimensional configuration was studied, the amplitude correction factor, Eq. (32), should be multiplied by π. The implementation of this background mean flow fields reformulation has successfully been verified for a sheared and stratified propagation medium [61].

3.3. Computing strategy and numerical parameters chosen

The adjoint formulation relies on a sensor based description of the propagation problem, it characterises how a point in the surrounding media would radiate towards the observer location if an elementary source of sound was placed there. Thus no distributed unsteady sound sources have to be mapped on the acoustic grid, instead a delta Dirac source is set at the microphone position $\mathbf{x}_m$. Extending the computational domain until the microphone location would make the numerical costs prohibitive, and a strategy to solve the propagation problem for a source set out of the domain is considered therefore. The idea, illustrated in Fig. 3, is to separate the acoustic propagation into two regions: a numerical domain containing the meaningful part of the jet flow for which adjoint Green's function is solved numerically, and the ambient region containing the adjoint source with possibly a uniform flow. The spherical waves emitted by the adjoint source are mapped analytically on the edge of the computational domain and adjoint Green's function is solved numerically on the domain interior.

The computational aeroacoustic grid that has been set up with Actran TM's built-in meshing tool. The mesh obtained with elements of size $0.1D_J$ is shown in Fig. 4. The physical domain is composed by a duct of diameter D_J and of length $5D_J$, from the

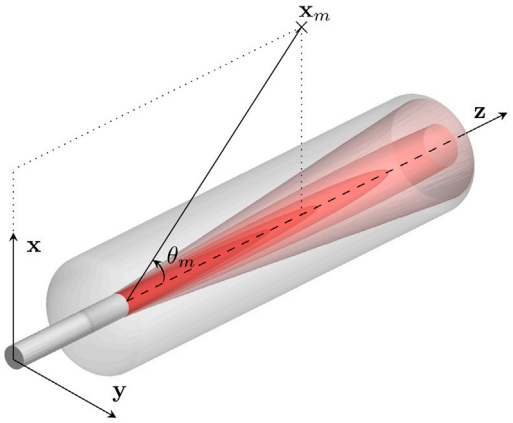

Fig. 3. Schematic representation of the propagation problem and definition of the reference frame. Adjoint Green's function $\phi^{\dagger(\mathbf{x}_s)}_{\mathbf{x}_m}$ is solved numerically for any $\mathbf{x}_s$ in the light grey volume where the flow is mapped.

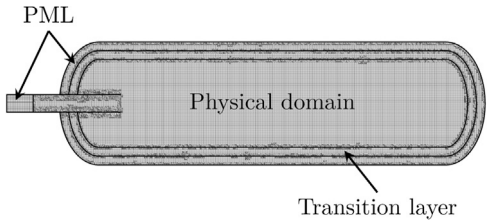

Fig. 4. Slice of the computational aeroacoustic grid with elements of size $0.1D_J$.

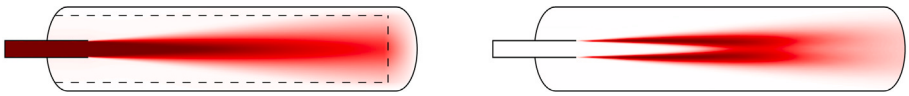

Fig. 5. Averaged Mach number M_0, and turbulent kinetic energy k computed from the large-eddy simulation and interpolated on the physical domain. $M_0 \in [0, 0.9]$ and $k \in [0, 5.6\times10^6]$. For $x^2 + y^2/D_J^2 \geq 4.0$ and $z/D_J \geq 18.0$ the mean velocity $\mathbf{u}_0$, mean density ρ_0 and mean pressure p_0 fields are smoothly cropped to fit their ambient value.

duct exhaust the domain is $20D_J$ long, and has a cylindrical shape with a radius of $2.5D_J$. The cylinder corners are rounded to avoid numerical singularities. The truncation of the domain is achieved with a $0.5D_J$ thick perfectly matched layer (PML). An additional PML region is added in the duct interior to simulate a semi-infinite conduit. A discussion on this specific in-duct boundary condition is given in Section 5.2.

It is not feasible to map on the boundary of the computational domain an incident field from a source set outside of this domain when the exterior flow is non-uniform. A $0.5D_J$ thick transition layer is built for this reason, to interface the physical domain and the non-reflecting boundary condition. The set of variables that characterise the propagation media, namely the mean velocity $\mathbf{u}_0$, the mean pressure p_0, the mean density ρ_0 or combinations of these fields are obtained from the averaging of a large-eddy simulation [44,48] and are mapped on the physical domain. A linear smoothing is applied on these mean flow fields for $x/D_J > 18$ and $r/D_J > 2$ so to match the uniform ambient values prescribed in the PML. This smoothing is visible on the Mach number field M_0 presented in Fig. 5. The interpolation of the turbulent kinetic energy k in this domain is also shown to illustrate that this region is sufficient large to contain all the relevant sources of mixing noise. Recall that the flow reversal theorem is used to compute adjoint Green's function [15, Eq. (9)], and that the mean flow fields that are mapped, have undergone the transformation described in Section 3.2 and are reversed with respect to the averaged LES solution.

Second order elements are found to enable a better cost/accuracy trade-off than first order ones [61] and are therefore considered here. To improve numerical performances, hexahedral elements are favoured over tetrahedral ones [62]. The mesh with quadratic elements of size $0.1D_J$ considered in this study possesses 7.7×10^6 degrees of freedom. Single precision is used to save half of the RAM requirements of the MUMPS solver, so that 75 GB of RAM and 6.5 h per frequencies were required to compute the solution. It is possible to chose alternative sparse system inversion algorithm with different RAM/CPU h trade-offs [63]. An Intel Skylake node with 32 cores 190 GB of RAM was used with 2 parallel tasks and 16 threads on each. The computation for 100 frequencies took around 40 h. The computation costs associated with this geometry, for different grid refinements are presented for the record in Table 1.

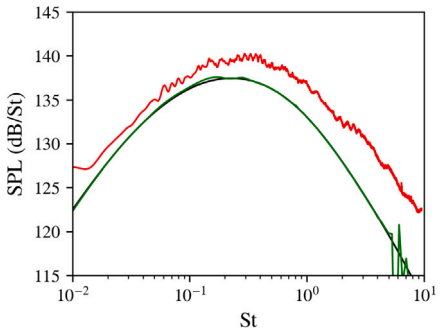

Fig. 6. Acoustic predictions at $\theta_m = 90°$. —— measurements [55], —— predictions with tailored adjoint Green's functions, and, —— predictions with analytical free-field Green's function from Eq. (26).

Table 1
Evolution of the computation costs with the grid refinement considering quadratic elements and MUMPS solver in single precision.

Size of elements	DOF	RAM requirements	Time for 100 freqs.
$0.5D_J$	0.2×10^6	1.8 GB	1.6 CPU h
$0.2D_J$	1.7×10^6	13 GB	62 CPU h
$0.1D_J$	7.7×10^6	75 GB	655 CPU h
$0.075D_J$	16.2×10^6	178 GB	5500 CPU h

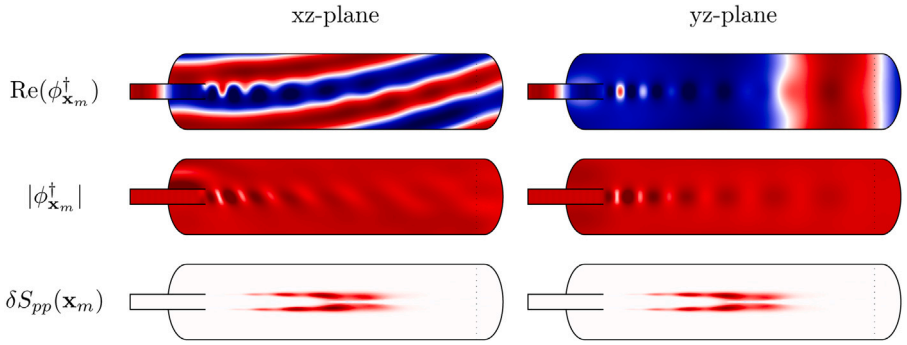

Fig. 7. Real part and absolute part of adjoint Green's function $\phi^\dagger_{\mathbf{x}_m}$ for an observer at $\theta_m = 90°$ and St = 0.3. The resulting modulation of the integrand $\delta S_{pp}(\mathbf{x}_m)$ is depicted. $\mathrm{Re}(\phi^\dagger_{\mathbf{x}_m}) \in [-3, 3] \times 10^{-6}$ Pa·s and $|\phi^\dagger_{\mathbf{x}_m}| \in [0, 4] \times 10^{-6}$ Pa·s.

4. Acoustic predictions at ninety degrees

Tam and Auriault's mixing noise formula is evaluated for an observer at ninety degrees from the jet axis. The reformulated expression given in Eq. (19) is considered. The receiver is located at a distance of $52D_J$ from the duct exit, this to mimic the acoustic far field conditions under study in [55]. The noise spectra over a Strouhal number interval ranging from 0.01 to 10 is calculated with a sampling of 100 adjoint Green's functions. Results are shown in Fig. 6.

The acoustic spectra obtained with the free field analytical solution and numerical adjoint Green's function overlap almost perfectly. Refraction effects were expected not to be of leading order at this observer angle [30,31], but the accuracy of this match is truly remarkable. The confidence in the methodology proposed is restricted by the refinement of the aeroacoustic grid and a criteria of number of points per wavelength. From the superposition of both curves, an upper limit for the confidence interval can be estimated, and for a mesh with elements of size $0.1D_J$ a good representation of the solution can be expected up to St~4.

The numerical solution allows to investigate in depth the behaviour of the adjoint solution. Details on the computation of the sound pressure level are provided here for the Strouhal numbers St = 0.3 and St = 0.9. The first value St = 0.3 corresponds to the Strouhal number for which the acoustic level is maximal, computed solutions are reported in Fig. 7. To illustrate the behaviour of adjoint fields at higher frequency, results for St = 0.9 are shown in Fig. 8.

These figures present visualisations in different cross-sections of the real part and the absolute part of adjoint Green's function $\phi^\dagger_{\mathbf{x}_m}$. The integrand $\delta S_{pp}(\mathbf{x}_m)$ of Tam and Auriault's formula, as given by Eq. (19), is also reproduced for these Strouhal numbers. It is the projection of adjoint Green's function on the turbulent mixing noise source model. In other words, this function filters the energy of the sound source by selecting the part that radiates toward the observer in weighting this contribution to include the

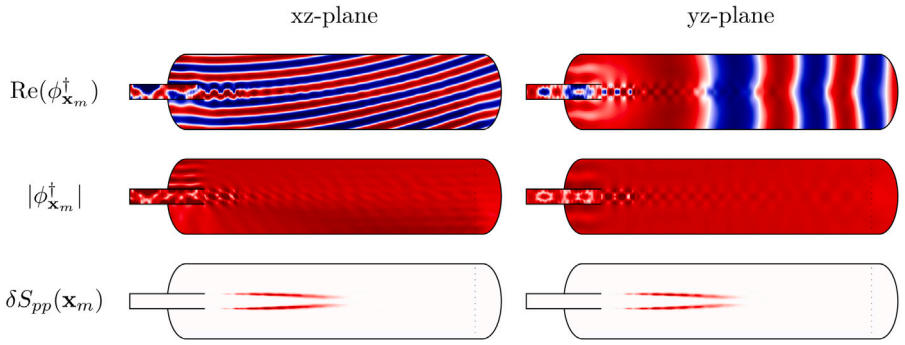

Fig. 8. Real part and absolute part of adjoint Green's function $\phi^{\dagger}_{\mathbf{x}_m}$ for an observer at $\theta_m = 90°$ and St = 0.9. The resulting modulation of the integrand $\delta S_{pp}(\mathbf{x}_m)$ is depicted. $\mathrm{Re}(\phi^{\dagger}_{\mathbf{x}_m}) \in [-3, 3] \times 10^{-6}$ Pa·s and $|\phi^{\dagger}_{\mathbf{x}_m}| \in [0, 4] \times 10^{-6}$ Pa·s.

acoustic propagation effects. Adjoint Green's function $\phi^{\dagger}_{\mathbf{x}_m}(\mathbf{x})$ accounts for all the propagation effects and indicates how effectively a source put in $\mathbf{x}$ would radiate to the observer $\mathbf{x}_m$, while $\delta S_{pp}(\mathbf{x}_m)$ represents the actual contribution at the observer position of the sound source. Note that within the present framework, sound generation and sound propagation are genuinely decoupled. In this sense the adjoint method shares the mindset of acoustic analogies and offers an interesting extension to the latter theory [16].

Even though it is seen in Fig. 6 that the acoustic noise spectra computed using tailored adjoint Green's functions closely follows the one obtained with free field analytical Green's functions, numerical Green's functions depicted in Figs. 7 and 8 present substantial differences with regard to their simplified analytical counterparts. This is most easily observed by considering the absolute values of both sets of Green's functions, and by recalling that from Eq. (26) the amplitude of the analytical solutions is roughly constant over the physical domain for an adjoint source set in the far field. An acoustic mode confined in the jet plume is clearly identified in Figs. 7 and 8, leading to a modulation of the integrand $\delta S_{pp}(\mathbf{x}_m)$ that is the scalar product of adjoint Green's function with the source term. Surprisingly enough, for the two Strouhal numbers considered and for this simple jet, St = 0.3 and St = 0.9, the acoustic energy received at ninety degrees from the jet axis originates slightly more from the shear layer area masked by the jet flow than from the area directly facing the observation point. The presence of the duct surface and the jet flow induce a scattered field. These results are reproduced for observers located at $\theta_m = 30°$ and $\theta_m = 150°$, and presented in Appendix D for the same Strouhal numbers values St = 0.3 and St = 0.9.

Discussing in details these adjoint solutions would go beyond the scope of this study which targets at presenting a methodology based on a stable formulation to compute sound propagation, and to calculate tailored adjoint Green's functions to predict jet noise. Note merely that the scalar product of adjoint Green's function on a sound source a priori as considered in this approach explicitly provides the actual contribution of a source of sound to a given observer location. With respect to previous formulations, the adjoint fields are easily accessible and computed in a robust manner. Note also that modal structures in the jet plume are almost absent for an observer located at $\theta_m = 30°$, they are visible at $\theta_m = 90°$ and very strong for an observer located upstream at $\theta_m = 150°$. What is more, the projection of these adjoint Green's functions on the sound source model makes clearly visible that various parts of the shear layer contribute at different observer angle.

5. Acoustic predictions in the upstream direction

Tailored adjoint Green's functions or analytically known free field Green's functions provide nearly identical predictions at ninety degrees. To illustrate the improvements in the predictions that can result from the use of tailored adjoint Green's functions, acoustic spectra computed at $\theta_m = 150°$ are presented. At this shallow angle, the emergence of tones in the acoustic far field spectrum has been reported and receive, since recently, a special attention in the literature [48,49,64,65]. It has been shown that these tones are related to the existence of guided jet waves inside the jet flow, and that despite their strong intensity, they are of purely acoustic nature.

Predictions obtained with the proposed model in considering numerical and analytical adjoint Green's functions computed over a sample of 200 Strouhal numbers are plotted in Fig. 9. The interested reader will find in Appendix D and in Appendix E visualisations of some tailored adjoint Green's functions which have been used for this calculation. The noise predictions are compared against the far field noise spectra measured for a Mach 0.9 isothermal round jet during the ECL test campaign [49]. Six tones are clearly visible in the sound pressure level calculated from the experiment at this grazing upstream angle. They are qualitatively reproduced in the prediction based on tailored adjoint Green's functions and absent from the noise spectra relying on the free field propagation model, indicating thereby that the tones are associated with purely sound propagation effects.

The amplitude of the tones are properly captured by the model within 2 dB. The first peak computed with tailored adjoint Green's functions is overestimated, while the third, the fourth and the fifth peak are a slightly underestimated. Above the frequency of the first tone, the broadband level of the acoustic spectra predicted is lower than the measured one, leading to higher peak-to-peak amplitudes in the prediction. It is seen in Fig. 9, that the most significant flaw in the prediction lies in the frequencies of the tones computed that are systematically lower than the measured ones. This point is addressed in what follows.

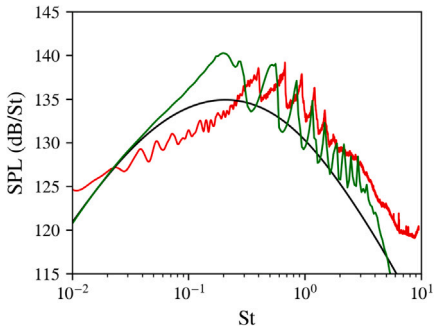

Fig. 9. Acoustic predictions at $\theta_m = 150°$. —— measurements [55], —— predictions with tailored adjoint Green's functions, and, —— predictions with analytical free-field Green's function from Eq. (26).

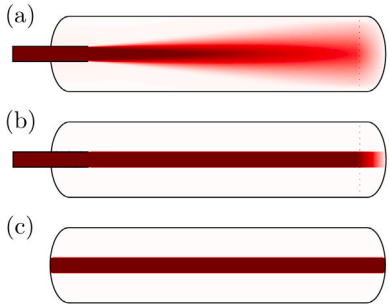

Fig. 10. Mach number M_0 considered for the computations of tailored adjoint Green's functions. The cases (a) and (b) include a portion of straight duct, from $z/D_J = 18.0$ downstream of the jet exhaust the mean flow is smoothed to ambient value. In (b) and (c), a plug flow with an infinitely thin shear layer is considered to fit into the assumption of the vortex sheet model. $M_0 \in [0, 0.9]$.

5.1. Influence of the flow and the geometry

Guided jet waves were first identified as the neutral wave modes of the jet. Tam and Ahuja [66] have shown that their mode shape as well as their frequency are correctly predicted by a cylindrical vortex sheet model. In order to get closer to the assumptions of their model, and attempt thereby to retrieve the correct tone frequencies, tailored adjoint Green's functions are computed for the two additional configurations displayed in Fig. 10. Fig. 10(a) represents the base flow considered in previous calculations. The configuration shown in Fig. 10(b) models the jet flow with a cylindrical plug flow exhausting from the semi-infinite straight duct. As in Fig. 10(a), the base flow in Fig. 10(b) is gradually restored to ambient values to enable a truncation of the numerical domain with minimal reflection at the boundary. A cylindrical plug flow with no solid surface that aims at best reproducing the hypothesis of the vortex sheet model is considered in Fig. 10(c). For this last configuration, the truncation of the numerical domain is achieved with three independent PML mapped with uniform flows.

Acoustic spectra at $\theta_m = 150°$ computed for these configurations over a sample of 200 Strouhal numbers are presented in Fig. 11. In all configurations, the sound sources are modelled identically to those of previous calculations, and hence, only the presence or absence of the pipe, the base flow, and the associated propagation effects differ in these computations. The prediction obtained for the case (a) is identical to the one presented Fig. 9 and reproduced for comparison. The acoustic results obtained with the infinitely thin shear layer model, the cases (b) and (c), are quite similar. The amplitude of the first three peaks increased with respect to the reference spectra corresponding to the case (a) as well as the peak-to-peak amplitude that is larger than 15 dB for cases (b) and (c). The tones are narrower, and the broadband level is more than 5 dB less energetic compared to the reference spectra. The reason for this substantial decrease of the broadband level is found in the recast of Tam and Auriault's model, in Eqs. (18) and (19), for which the exponential in the integrand filters out any contribution of the sound source when $u_0 \to 0$. That is for the plug flow of case (b) and (c), only the part of the sound source in the flow effectively contribute to the total sound pressure level. It is however seen from Fig. 11, that the position of the peaks are not significantly modified, indicating a fairly high robustness of the peak position with respect to the jet flow profile [48] and geometry. Adjoint Green's functions tailored to these three configurations are presented in Appendix E, and their structure for the first three tones are also briefly discussed. It comes out, that the length of the jet potential core, the shear layer thickness as well as the presence of the nozzle are not sufficient to recover the correct frequencies of the tones.

5.2. Influence of the in-duct boundary condition

Acoustic modes in the jet plume are visible in tailored adjoint Green's functions computed for observers located in the upstream direction. This is illustrated in Appendix E for an observer at $\theta_m = 150°$. At the conduit exhaust these modal structures interface

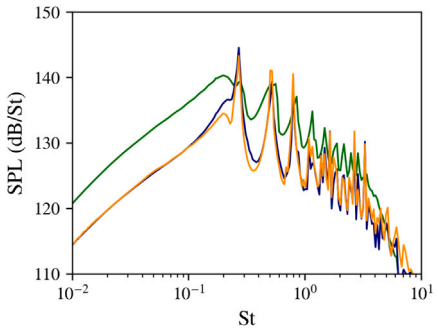

Fig. 11. Acoustic predictions at $\theta_m = 150°$ for the configurations presented in Fig. 10. case (a), case (b), and, case (c).

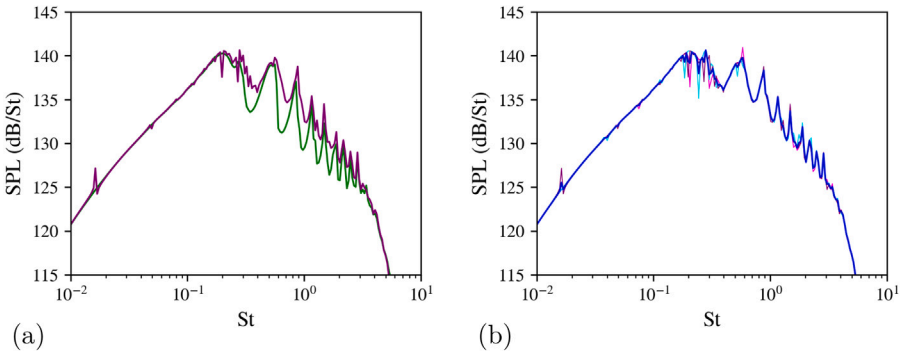

Fig. 12. Acoustic predictions at $\theta_m = 150°$. (a), predictions with the semi-infinite duct model, and with a fully reflective duct of length $5D_J$. (b), predictions with a fully reflective duct, , of length D_J, , of length $2D_J$, and, , of length $5D_J$. , noise spectra computed from the averaging of the three predictions with different duct length.

with the duct modes, so that an influence of the nozzle impedance on adjoint Green's function computed in the jet potential core can be expected.

So far, the duct has been modelled as semi-infinite by considering a PML, and the value of the reflection coefficient in the duct is low. This contrasts with laboratory tests for which ducts have finite length, and are reflective. This reflection in the conduit needs to be accounted for in the global stability analysis of trapped acoustic modes as shown by Schmidt et al. [67, Appendix B] to retrieve the correct envelope of the least damped global mode. It is moreover known that changing a non-reflecting boundary condition to a partially reflecting one shifts the eigenfrequencies of resonators [68], and a modification of the nozzle impedance may influence the tone frequencies of upstream-propagating guided jet modes in a similar fashion.

Since the nozzle impedance is unknown, a simple hard-wall boundary condition ($u'_z = 0$) that is permeable to the flow ($u_{0,z} \neq 0$) is considered in what follows to mimic the finite duct length and its internal reflection. Fig. 12(a) compares the acoustic prediction obtained with the semi-infinite duct model and the one assuming a finite length duct. Taking into account the duct internal reflection as for an effect to increase slightly the tone frequencies and to widen the peaks. With respect to the predictions obtained with the semi-infinite duct model, the falling edge of the tone occurs for a Strouhal number increased by roughly 0.1, but the rising edge of the tone is unchanged. The amplitude of the peaks remain globally identical, except for the fifth peak that is increased by approximately 3 dB. The sound pressure level minima between the peaks are also 3–5 dB more energetic. For Strouhal numbers lower than St = 0.4, the acoustic spectra presents series of peaks, the frequency of which are harmonics of the quarter wave resonator formed by the duct cavity [69]. Experiments on the acoustic resonance of an open-ended duct [70] have shown that such resonances of a duct in flow are almost completely suppressed by losses when the flow Mach number exceeds $M = 0.4$. To remove these peaks, three computations with ducts of length D_J, $2D_J$ and $5D_J$ are considered, and their acoustic spectra averaged. Fig. 12(b) displays the thereby obtained averaged acoustic spectra as well as the three individual predictions made for that purpose. The tones identified previously as guided jet waves are not significantly altered, while the other events associated with the duct resonance are smoothed. In addition, the amplitude of the fifth tone returned to a level similar to the one obtained with a semi-infinite duct model.

This acoustic spectra obtained from averaging of the predictions computed for different duct lengths gives an estimate of the sound pressure level that would be obtained if the duct internal reflection would be accounted for in the sound propagation. Fig. 13 compares this acoustic spectra with measurements and predictions that consider the duct as semi-infinite. Predictions associated with a free field propagation of Tam and Auriault's mixing noise are given for the record. The tone frequencies predicted by accounting for the in-duct reflections matches now much better with the measured ones. The noise spectra computed by accounting for in-duct reflections is also systematically louder that the solution considering free field propagation. For the semi-infinite duct model, minima

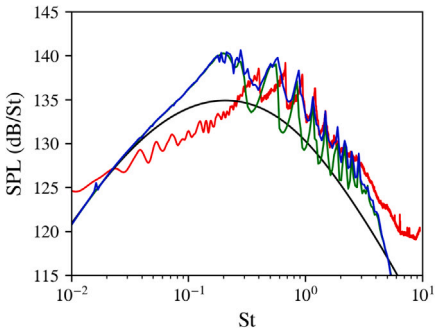

Fig. 13. Acoustic predictions at $\theta_m = 150°$. ——, measurements [55], ——, predictions assuming the duct is semi-infinite, ——, predictions modelling the duct internal reflection, and ——, predictions with analytical free-field Green's function from Eq. (26).

between peaks are lower than their counterpart that assume free field propagation, suggesting that some acoustic energy possibly leaks out through the duct at these frequencies.

6. Far field acoustic spectra with a duct of finite length

The effect of accounting for in-duct reflections is now investigated for other polar angles. Fig. 14 presents the acoustic spectra computed for observers located at angles from $\theta_m = 30°$ to $\theta_m = 140°$. As previously, to remove the non-physical duct quarter wave resonances, adjoint Green's functions are computed in assuming a total in-duct reflection of the acoustics for three duct lengths. An averaging of the resulting spectra is then considered.

The emergence of guided jet waves are visible for the predictions that consider tailored adjoint Green's functions at the polar angles $\theta_m = 120°$, $\theta_m = 130°$ and $\theta_m = 140°$, which are displayed in Fig. 14(d) to (f). At these angles the dynamic of the tones are correctly predicted within a tolerance of 3 dB for a decade of Strouhal number between St = 0.2 and St = 2.0. The tones are about 5 dB more energetic when in-duct reflections are modelled, and, as for previous computation at $\theta_m = 150°$, their position is also better predicted when in-duct reflections are modelled. This confirms the importance of accounting for the nozzle impedance to correctly predict these events.

Although the model is reasonably successful in capturing noise levels above $\theta_m = 120°$ in this decade of Strouhal number, the predicted spectra underestimate the measurements as the observer moves away from these angles. At $\theta_m = 90°$, measured levels are under-predicted by 2 dB, at $\theta_m = 60°$, 5 dB are missing, and at $\theta_m = 30°$, the gap is as large as 17 dB. The downstream polar angles are dominated by the radiation of large turbulent scales [39] which are not included in Tam and Auriault's mixing noise model. Thus it is not surprising that the model fails at predicting the correct amplitudes at these angles. A more complete modelling of the Reynolds stress tensor than that of Eq. (7) seems also able to consistently retrieve the correct polar directivity [5,53]. Investigating alternative noise source models [9,18,19] may thus correct this trend.

At $\theta_m = 130°$, $\theta_m = 140°$ and $\theta_m = 150°$, the low frequency spectra is overestimated independently of the sound propagation model considered indicating an imperfection of the model proposed here. At these upstream shallow angles, a hump centred around St = 0.1 emerges in the noise spectra computed from tailored Green's functions. The latter is predicted equally by modelling the duct as semi-infinite or as totally reflecting, but it is absent from the measurements and from the predictions that assume free field propagation. The amplitude of this peak increases as the observer moves upstream and that it finally merges with the first tone of the upstream-propagating guided jet wave. The origin of this phenomena is presently unknown and deserves further investigation.

At $\theta_m = 30°$, the acoustic spectrum computed considering tailored adjoint Green's functions are significantly narrower than their free field counterpart. This is a well-known consequence of acoustic refraction, yet what is remarkable is that the shape of the $\theta_m = 30°$ degree measured spectrum is thereby retrieved. Noise spectra computed without modelling in-duct reflections closely follow the predictions achieved with the free field analytical model from $\theta_m = 60°$ to $\theta_m = 130°$ in a noteworthy way. All acoustic predictions overlap for Strouhal numbers lower than St = 0.1. Above this threshold, predictions are sensitive to the methodology used to propagate sound. It is seen that the acoustic predictions that account for in-duct reflections are systematically more energetic than those obtained with a semi-infinite duct model. For Strouhal numbers greater than St = 0.3, this extra acoustic energy is spread over more than one decade of Strouhal number, and is of the order of 2–3 dB. This amount of energy is considerable.

7. Conclusion

This study reformulates Tam and Auriault's mixing noise model for Pierce's wave equation, and solves numerically adjoint Green's functions associated with the jet noise propagation problem. The benefits of this new formulation are twofold; the acoustic propagation problem is made unconditionally stable and the adjoint solution to the propagation problem can be solved using the convenient flow reversal theorem. The commercial solver `Actran TM` is used to compute adjoint Green's functions that are tailored to the geometry and the flow of the subsonic jet under consideration. Noise predictions with a reasonably fine frequency discretisation are obtained in computing time of the order of one day.

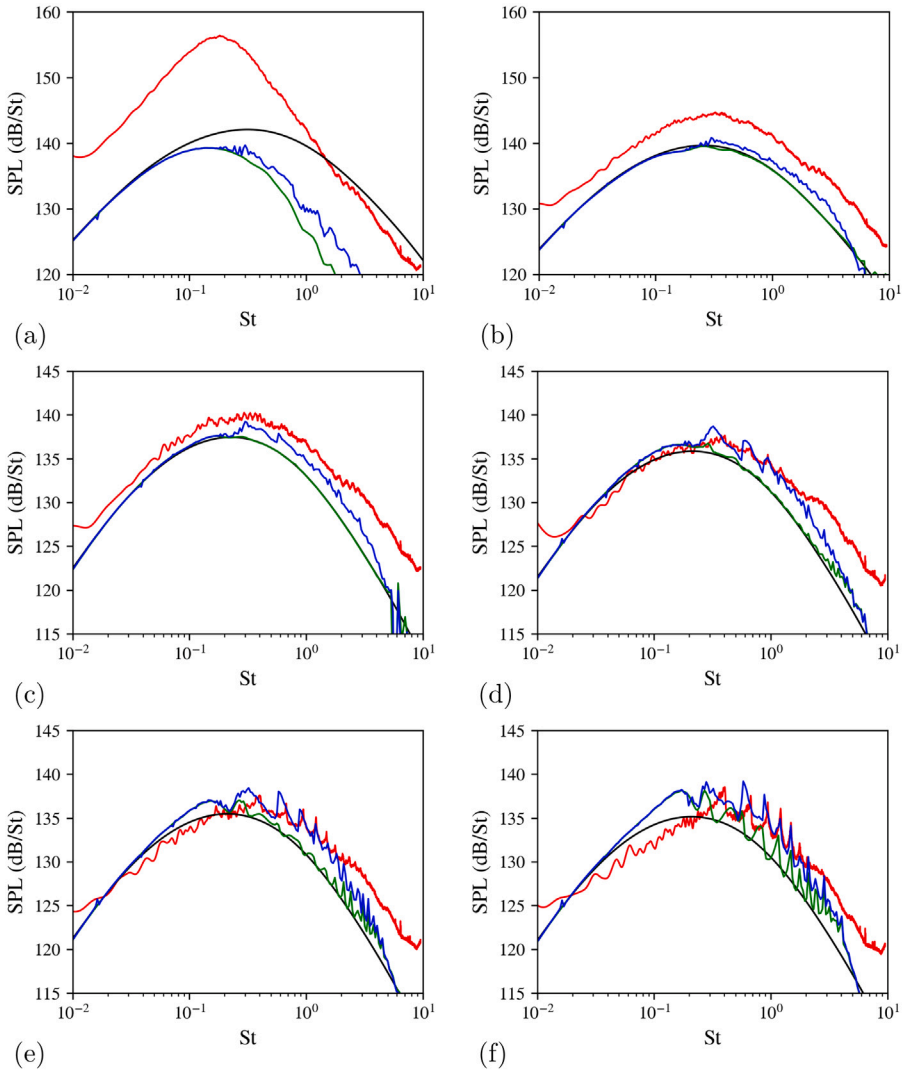

Fig. 14. Acoustic predictions at, (a) $\theta_m = 30°$, (b) $\theta_m = 60°$, (c) $\theta_m = 90°$, (d) $\theta_m = 120°$, (e) $\theta_m = 130°$ and (f) $\theta_m = 140°$. ——, measurements [55], ——, predictions assuming the duct is semi-infinite, ——, predictions modelling the duct internal reflection, and ——, predictions with analytical free-field Green's function from Eq. (26).

Within a noise prediction strategy based on acoustic analogies, there are features related to sound propagation in jets, such as upstream propagating guided jet waves, that tailored adjoint Green's functions can describe with some success. Deviations have been observed between the frequencies of the tones measured and those predicted assuming a semi-infinite duct model. Investigations at constant jet Mach number have shown that the position of these peaks are not very sensitive to the structure of the jet plume, but are strongly influenced by the impedance of the conduit. Considering a total reflection of the acoustic energy in the duct broadens the descending fronts of the tone associated with the jet neutral mode, and give peak positions more in line with what is measured.

Tam and Auriault's prediction model for turbulent mixing noise is unable to describe the acoustic directivity in the downstream direction, but encounters also limitations in the upstream arc. Effort in consistently redrafting a noise source model can be undertaken, now that some confidence is gained in the computation of sound propagation effects with help of tailored adjoint Green's functions. An effort will be made to address this specific point.

In an acoustic analogy framework, the radiating part of the sound source is filtered by Green's functions. The adjoint isolates this contribution and weights the source intensity by taking into account the acoustic path from the source to the listener. Starting from a source model, the adjoint allows to characterise its contribution to the sound received by a given observer, and thus, gives indication on the localisation of the radiating part of sound sources. It is seen that the way in which shear layers radiate depends on the point of observation. At some frequencies, the sound field which radiates downstream of the jet does not pass through the jet, but comes mainly from the shear layer that is directly visible from the observation point. Upstream, the opposite is true, adjoint Green's functions indicates that it is more the part of the shear layer hidden by the jet that contributes to the listener position.

Data availability

Data will be made available on request.

Acknowledgements

The authors would like to thank César Legendre for his expert and constant support in setting up the calculations in Actran TM. The first author benefited from insightful discussions on the physics of guided jet modes with Mathieu Varé. This work was performed within the framework of the AMBROSIA project founded by The French Civil Aviation Authority (DGAC Convention 2019-18), with also the support of the Labex CeLyA of the Université de Lyon, within the programme "Investissements d'Avenir" (ANR-10-LABX-0060/ANR-16-IDEX-0005) operated by the French National Research Agency (ANR). This work was granted access to the HPC resources of PMCS2I (Pôle de Modélisation et de Calcul en Sciences de l'Ingénieur de l'Information) of École Centrale de Lyon.

Appendix A. Conventions and formulae

A.1. Definition of the pressure autocorrelation

The pressure autocorrelation $R_{pp}(\mathbf{x}_m,\tau)$ at a position $\mathbf{x}_m$ and for a time separation τ is by definition, $R_{pp}(\mathbf{x}_m,\tau) \equiv \overline{p(\mathbf{x}_m,\bullet)p(\mathbf{x}_m,\bullet+\tau)}$, with,

$$\overline{p(\mathbf{x}_m,\bullet)p(\mathbf{x}_m,\bullet+\tau)} = \lim_{T\to\infty}\frac{1}{T}\int_{-T/2}^{T/2}\mathrm{d}t_m\ \ p(\mathbf{x}_m,t_m)p(\mathbf{x}_m,t_m+\tau) \tag{A.1}$$

A.2. Convention for the Fourier transform

A non-unitary Fourier transform in time is considered in this study,

$$F(\mathbf{x},\omega) = \int_{\mathbb{R}}\mathrm{d}t\ f(\mathbf{x},t)e^{\mathrm{i}\,\omega t} \qquad \text{and} \qquad f(\mathbf{x},t) = \frac{1}{2\pi}\int_{\mathbb{R}}\mathrm{d}\omega\ F(\mathbf{x},\omega)e^{-\mathrm{i}\,\omega t} \tag{A.2}$$

Source-observer Green's function is defined in the frequency domain as $G_{\mathbf{x}_s}^{(\mathbf{x}_m,\omega)}$ and in the time domain as $g_{\mathbf{x}_s,t_s}^{(\mathbf{x}_m,t_m)} \equiv g_{\mathbf{x}_s}^{(\mathbf{x}_m,\tau)}$, with $\tau \equiv t_m - t_s$. The time Fourier transform definition for Green's function chosen for this study writes,

$$G_{\mathbf{x}_s}^{(\mathbf{x}_m,\omega)} = \int_{\mathbb{R}}\mathrm{d}\tau\ g_{\mathbf{x}_s}^{(\mathbf{x}_m,\tau)}e^{\mathrm{i}\,\omega\tau} = \int_{\mathbb{R}}\mathrm{d}\tau\ g_{\mathbf{x}_s,t_s}^{(\mathbf{x}_m,t_s+\tau)}e^{\mathrm{i}\,\omega\tau} \tag{A.3}$$

and,

$$g_{\mathbf{x}_s,t_s}^{(\mathbf{x}_m,t_m)} = g_{\mathbf{x}_s}^{(\mathbf{x}_m,\tau)} = \frac{1}{2\pi}\int_{\mathbb{R}}\mathrm{d}\omega\ G_{\mathbf{x}_s}^{(\mathbf{x}_m,\omega)}e^{-\mathrm{i}\,\omega\tau} \tag{A.4}$$

A.3. Choice of the scalar product

The scalar product of two real valued vectors $\mathbf{a}$ and $\mathbf{b}$ is defined on a space Ω as,

$$\langle\mathbf{a},\mathbf{b}\rangle\ =\ \int_{\Omega}\mathrm{d}\mathbf{x}\int_{\mathbb{R}}\mathrm{d}t\ \mathbf{a}(\mathbf{x},t)\cdot\mathbf{b}(\mathbf{x},t) \tag{A.5}$$

A.4. Integration formulae

The reformulation of Tam and Auriault's mixing noise model has recourse to the following formulas.
For $\mathrm{Re}(\mu) > 0$,

$$\int_{\mathbb{R}}\mathrm{d}x\ \exp\left(-\mu x^2\right) = \sqrt{\frac{\pi}{\mu}} \tag{A.6}$$

$$\int_{\mathbb{R}}\mathrm{d}x\ x\exp\left(-\mu x^2\right) = 0 \tag{A.7}$$

For $\mathrm{Re}(\mu)+\mathrm{Im}(\nu) > 0$,

$$\int_{\mathbb{R}}\mathrm{d}x\ \exp\left(-\mu|x|+\mathrm{i}\,\nu x\right) = \frac{1}{\mu-\mathrm{i}\,\nu}+\frac{1}{\mu+\mathrm{i}\,\nu} = \frac{2\mu}{\mu^2+\nu^2} \tag{A.8}$$

$$\int_{\mathbb{R}}\mathrm{d}x\ x\exp\left(-\mu|x|+\mathrm{i}\,\nu x\right) = \frac{1}{(\mu-\mathrm{i}\,\nu)^2}-\frac{1}{(\mu+\mathrm{i}\,\nu)^2} = \frac{4\mathrm{i}\,\mu\nu}{(\mu^2+\nu^2)^2} \tag{A.9}$$

Integral computation found in [71, Eq. (3.323), p.337 in 7th ed.] for $\mathrm{Re}(p^2) > 0$,

$$\int_{\mathbb{R}}\mathrm{d}x\ \exp\left(-p^2x^2\pm qx\right) = \frac{\sqrt{\pi}}{p}\exp\left(\frac{q^2}{4p^2}\right) \tag{A.10}$$

Appendix B. Details on the derivations

This section presents the details of the reformulation of Tam and Auriault's mixing noise model, where, for the sake of concision, the pressure autocorrelation R_{pp} is considered as starting point instead of its Fourier transform, the noise spectrum S_{pp}.

B.1. Calculation of the acoustic noise spectra

The pressure autocorrelation expressed with Pierce's wave equation writes,

$$R_{pp}(\mathbf{x}_m,\tau)=\overline{\frac{\mathrm{D}(\phi)}{\mathrm{D}_{\bullet,\mathbf{x}_m}}\frac{\mathrm{D}(\phi)}{\mathrm{D}_{\bullet+\tau,\mathbf{x}_m}}} \tag{B.1}$$

or more explicitly,

$$R_{pp}(\mathbf{x}_m,\tau)=\lim_{T\to\infty}\frac{1}{T}\int_{-T/2}^{T/2}\mathrm{d}t_m\ \frac{\mathrm{D}(\phi)}{\mathrm{D}_{t_m,\mathbf{x}_m}}\frac{\mathrm{D}(\phi)}{\mathrm{D}_{t_m+\tau,\mathbf{x}_m}} \tag{B.2}$$

Recasting ϕ with Lagrange's identity furnishes,

$$R_{pp}(\mathbf{x}_m,\tau)=\lim_{T\to\infty}\frac{1}{T}\int_{-T/2}^{T/2}\mathrm{d}t_m\ \frac{\mathrm{D}}{\mathrm{D}_{t_m,\mathbf{x}_m}}\left[\int_\Omega\mathrm{d}\mathbf{x}_1\int_{\mathbb{R}}\mathrm{d}t_1\ \phi^\dagger_{\mathbf{x}_m,t_m}(\mathbf{x}_1,t_1)\frac{\mathrm{D}(q_s(\mathbf{x}_1,t_1))}{\mathrm{D}_{t_1,\mathbf{x}_1}}\right]\frac{\mathrm{D}}{\mathrm{D}_{t_m+\tau,\mathbf{x}_m}}\left[\int_\Omega\mathrm{d}\mathbf{x}_2\int_{\mathbb{R}}\mathrm{d}t_2\ \phi^\dagger_{\mathbf{x}_m,t_m+\tau}(\mathbf{x}_2,t_2)\frac{\mathrm{D}(q_s(\mathbf{x}_2,t_2))}{\mathrm{D}_{t_2,\mathbf{x}_2}}\right] \tag{B.3}$$

Because τ is constant with respect to t_m, $\mathrm{D}/\mathrm{D}_{t_m+\tau,\mathbf{x}_m}=\mathrm{D}/\mathrm{D}_{t_m,\mathbf{x}_m}$, moreover $\mathbf{x}_1$, $\mathbf{x}_2$, t_1 and t_2 are independent of $\mathbf{x}_m$ and t_m, so that previous material derivatives only applies on the $\phi^\dagger$ fields leading to,

$$R_{pp}(\mathbf{x}_m,\tau)=\lim_{T\to\infty}\frac{1}{T}\int_{-T/2}^{T/2}\mathrm{d}t_m\int_\Omega\mathrm{d}\mathbf{x}_1\int_\Omega\mathrm{d}\mathbf{x}_2\int_{\mathbb{R}}\mathrm{d}t_1\int_{\mathbb{R}}\mathrm{d}t_2\ \frac{\mathrm{D}\left(\phi^\dagger_{\mathbf{x}_m,t_m}(\mathbf{x}_1,t_1)\right)}{\mathrm{D}_{t_m,\mathbf{x}_m}}\frac{\mathrm{D}\left(\phi^\dagger_{\mathbf{x}_m,t_m+\tau}(\mathbf{x}_2,t_2)\right)}{\mathrm{D}_{t_m,\mathbf{x}_m}}\frac{\mathrm{D}(q_s(\mathbf{x}_1,t_1))}{\mathrm{D}_{t_1,\mathbf{x}_1}}\frac{\mathrm{D}(q_s(\mathbf{x}_2,t_2))}{\mathrm{D}_{t_2,\mathbf{x}_2}} \tag{B.4}$$

Recalling the equivalent notation for Green's functions, $G^{(\mathbf{x}_m,t_m)}_{\mathbf{x}_s,t_s}\equiv G^{(\mathbf{x}_m,t_m-t_s)}_{\mathbf{x}_s}$, and applying to t_1 and t_2 the change of variable $\tilde{t}_1\equiv t_1-t_m$ and $\tilde{t}_2\equiv t_2-t_m$ gives,

$$R_{pp}(\mathbf{x}_m,\tau)=\lim_{T\to\infty}\frac{1}{T}\int_{-T/2}^{T/2}\mathrm{d}t_m\int_\Omega\mathrm{d}\mathbf{x}_1\int_\Omega\mathrm{d}\mathbf{x}_2\int_{\mathbb{R}}\mathrm{d}\tilde{t}_1\int_{\mathbb{R}}\mathrm{d}\tilde{t}_2\ \frac{\mathrm{D}\left(\phi^\dagger_{\mathbf{x}_m}(\mathbf{x}_1,\tilde{t}_1)\right)}{\mathrm{D}_{t_m,\mathbf{x}_m}}\frac{\mathrm{D}\left(\phi^\dagger_{\mathbf{x}_m}(\mathbf{x}_2,\tilde{t}_2-\tau)\right)}{\mathrm{D}_{t_m,\mathbf{x}_m}}\frac{\mathrm{D}(q_s(\mathbf{x}_1,\tilde{t}_1+t_m))}{\mathrm{D}_{\tilde{t}_1+t_m,\mathbf{x}_1}}\frac{\mathrm{D}(q_s(\mathbf{x}_2,\tilde{t}_2+t_m))}{\mathrm{D}_{\tilde{t}_2+t_m,\mathbf{x}_2}} \tag{B.5}$$

Due to the time-shift invariance of $\phi^\dagger_{\mathbf{x}_m}$, their material derivatives can be expressed as function of $\tilde{t}_1$ and $\tilde{t}_2$,

$$\begin{aligned}\frac{\partial}{\partial t_m}\phi^\dagger_{\mathbf{x}_m}(\mathbf{x}_1,\tilde{t}_1)&=\frac{\partial}{\partial t_m}\phi^\dagger_{\mathbf{x}_m}(\mathbf{x}_1,t_1-t_m)\\&=-\frac{\partial}{\partial(t_1-t_m)}\phi^\dagger_{\mathbf{x}_m}(\mathbf{x}_1,t_1-t_m)\\&=-\frac{\partial}{\partial\tilde{t}_1}\phi^\dagger_{\mathbf{x}_m}(\mathbf{x}_1,\tilde{t}_1)\end{aligned} \tag{B.6}$$

and similarly,

$$\frac{\partial}{\partial t_m}\phi^\dagger_{\mathbf{x}_m}(\mathbf{x}_2,\tilde{t}_2-\tau)=-\frac{\partial}{\partial\tilde{t}_2}\phi^\dagger_{\mathbf{x}_m}(\mathbf{x}_2,\tilde{t}_2-\tau) \tag{B.7}$$

Since $\tilde{t}_1$ and $\tilde{t}_2$ are independent of t_m the pressure time autocorrelation R_{pp} rewrites as,

$$R_{pp}(\mathbf{x}_m,\tau)=\int_\Omega\mathrm{d}\mathbf{x}_1\int_\Omega\mathrm{d}\mathbf{x}_2\int_{\mathbb{R}}\mathrm{d}\tilde{t}_1\int_{\mathbb{R}}\mathrm{d}\tilde{t}_2\ \frac{\mathrm{D}\left(\phi^\dagger_{\mathbf{x}_m}(\mathbf{x}_1,\tilde{t}_1)\right)}{\mathrm{D}_{-\tilde{t}_1,\mathbf{x}_m}}\frac{\mathrm{D}\left(\phi^\dagger_{\mathbf{x}_m}(\mathbf{x}_2,\tilde{t}_2-\tau)\right)}{\mathrm{D}_{-\tilde{t}_2,\mathbf{x}_m}}\lim_{T\to\infty}\frac{1}{T}\int_{-T/2}^{T/2}\mathrm{d}t_m\ \frac{\mathrm{D}(q_s(\mathbf{x}_1,\tilde{t}_1+t_m))}{\mathrm{D}_{t_m,\mathbf{x}_1}}\frac{\mathrm{D}(q_s(\mathbf{x}_2,\tilde{t}_2+t_m))}{\mathrm{D}_{t_m,\mathbf{x}_2}} \tag{B.8}$$

Eventually, the change of variables $\tilde{t}_m\equiv t_m+\tilde{t}_2$ and $\tilde{\tau}\equiv\tilde{t}_1-\tilde{t}_2=t_1-t_2$ allows to retrieve the Q-term space–time correlation R_{QQ} defined as,

$$R_{QQ}(\mathbf{x}_1,\mathbf{x}_2,\tilde{\tau})\equiv\lim_{T\to\infty}\frac{1}{T}\int_{-T/2}^{T/2}\mathrm{d}\tilde{t}_m\ \frac{\mathrm{D}(q_s(\mathbf{x}_1,\tilde{t}_m+\tilde{\tau}))}{\mathrm{D}_{\tilde{t}_m,\mathbf{x}_1}}\frac{\mathrm{D}(q_s(\mathbf{x}_2,\tilde{t}_m))}{\mathrm{D}_{\tilde{t}_m,\mathbf{x}_2}} \tag{B.9}$$

or with an alternative notation,

$$R_{QQ}(\mathbf{x}_1,\mathbf{x}_2,\tilde{\tau})\equiv\overline{\frac{\mathrm{D}(q_s(\mathbf{x}_1,\bullet+\tilde{\tau}))}{\mathrm{D}_{\bullet,\mathbf{x}_1}}\frac{\mathrm{D}(q_s(\mathbf{x}_2,\bullet))}{\mathrm{D}_{\bullet,\mathbf{x}_2}}} \tag{B.10}$$

As previously, the Fourier transformed pressure autocorrelation S_{pp} can be computed, and after decomposing in the Fourier space the material derivatives of $\phi^{\dagger}_{\mathbf{x}_m}$, i.e.

$$\begin{aligned}\frac{\mathrm{D}\left(\phi^{\dagger(\mathbf{x}_1,\tilde{t}_1)}_{\mathbf{x}_m}\right)}{\mathrm{D}_{-\tilde{t}_1,\mathbf{x}_m}} &= \int_{\mathbb{R}} \frac{\mathrm{d}\omega_1}{2\pi}\left(\mathrm{i}\,\omega_1\phi^{\dagger(\mathbf{x}_1,\omega_1)}_{\mathbf{x}_m} + \mathbf{u}_0\cdot\nabla\phi^{\dagger(\mathbf{x}_1,\omega_1)}_{\mathbf{x}_m}\right)e^{-\mathrm{i}\,\omega_1\tilde{t}_1}\\ &= -\int_{\mathbb{R}} \frac{\mathrm{d}\omega_1}{2\pi}\mathrm{D}_{-\mathbf{u}_0,\mathbf{x}_m}\left(\phi^{\dagger(\mathbf{x}_1,\omega_1)}_{\mathbf{x}_m}\right)e^{-\mathrm{i}\,\omega_1\tilde{t}_1}\end{aligned} \tag{B.11}$$

in a similar fashion,

$$\frac{\mathrm{D}\left(\phi^{\dagger(\mathbf{x}_2,\tilde{t}_2-\tau)}_{\mathbf{x}_m}\right)}{\mathrm{D}_{-\tilde{t}_2,\mathbf{x}_m}} = -\int_{\mathbb{R}} \frac{\mathrm{d}\omega_2}{2\pi}\mathrm{D}_{-\mathbf{u}_0,\mathbf{x}_m}\left(\phi^{\dagger(\mathbf{x}_2,\omega_2)}_{\mathbf{x}_m}\right)e^{-\mathrm{i}\,\omega_2(\tilde{t}_2-\tau)} \tag{B.12}$$

where $\mathrm{D}_{\mathbf{u}_0,\mathbf{x}_m}$ is the material derivative along $\mathbf{u}_0$ taken at the position $\mathbf{x}_m$ and expressed in the frequency domain. Additional variables in index refer to position or frequency for which the material derivative applies. After integrating over τ by recalling,

$$\int_{\mathbb{R}} \mathrm{d}\tau\; e^{\mathrm{i}\,(\omega+\omega_2)\tau} = 2\pi\delta(\omega+\omega_2) \tag{B.13}$$

following formula is obtained for the acoustic spectral density S_{pp},

$$S_{pp}(\mathbf{x}_m,\omega) = \frac{1}{2\pi}\int_{\Omega}\mathrm{d}\mathbf{x}_1\int_{\Omega}\mathrm{d}\mathbf{x}_2\int_{\mathbb{R}}\mathrm{d}\tilde{t}_1\int_{\mathbb{R}}\mathrm{d}\tilde{t}_2\int_{\mathbb{R}}\mathrm{d}\omega_1\int_{\mathbb{R}}\mathrm{d}\omega_2\;\mathrm{D}_{-\mathbf{u}_0,\mathbf{x}_m}\left(\phi^{\dagger(\mathbf{x}_1,\omega_1)}_{\mathbf{x}_m}\right)\mathrm{D}_{-\mathbf{u}_0,\mathbf{x}_m}\left(\phi^{\dagger(\mathbf{x}_2,\omega_2)}_{\mathbf{x}_m}\right)e^{-\mathrm{i}\,\omega_1\tilde{t}_1-\mathrm{i}\,\omega_2\tilde{t}_2}R_{QQ}(\mathbf{x}_1,\mathbf{x}_2,\tilde{t}_1-\tilde{t}_2)\delta(\omega+\omega_2) \tag{B.14}$$

The straightforward evaluation of the integral over ω_2 along with the change of variable $\tilde{t}_2 = \tilde{t}_1 - \tilde{\tau}$ are performed,

$$S_{pp}(\mathbf{x}_m,\omega) = \int_{\Omega}\mathrm{d}\mathbf{x}_1\int_{\Omega}\mathrm{d}\mathbf{x}_2\int_{\mathbb{R}}\mathrm{d}\tilde{t}_1\int_{\mathbb{R}}\mathrm{d}\tilde{\tau}\int_{\mathbb{R}}\mathrm{d}\omega_1\;\mathrm{D}_{-\mathbf{u}_0,\mathbf{x}_m}\left(\phi^{\dagger(\mathbf{x}_1,\omega_1)}_{\mathbf{x}_m}\right)\mathrm{D}_{-\mathbf{u}_0,\mathbf{x}_m}\left(\phi^{\dagger(\mathbf{x}_2,-\omega)}_{\mathbf{x}_m}\right)\frac{e^{-\mathrm{i}\,\tilde{t}_1(\omega_1-\omega)}}{2\pi}e^{-\mathrm{i}\,\omega\tilde{\tau}}R_{QQ}(\mathbf{x}_1,\mathbf{x}_2,\tilde{\tau}) \tag{B.15}$$

which leads to Eq. (14) by the successive integrations over $\tilde{t}_1$ and ω_1.

B.2. Fraunhofer's approximation

Fraunhofer's approximation considered here,

$$\phi^{\dagger(\mathbf{r}+\mathbf{x}_2,\omega)}_{\mathbf{x}_m} \approx \phi^{\dagger(\mathbf{x}_2,\omega)}_{\mathbf{x}_m}\exp\left(\frac{\mathrm{i}\,\omega\;\mathbf{x}_m\cdot\mathbf{r}}{a_\infty|\mathbf{x}_m|}\right) \tag{B.16}$$

differs from the one found in the literature [4], [21, Eq. (14)] by the sign of the phase-shift. This is due to the differences in reciprocity principle used by Tam and Auriault [17, Eq. (2)] and by the authors [15, Eq. (B5)]. Details on this formula are given in what follows. Only the difference in travel time between rays is accounted for, so that the ray coming from $\mathbf{x}_2$ is the same as the one from $\mathbf{x}_2+\mathbf{r}$ but with an additional phase $\varphi = \mathbf{k}\cdot\mathbf{r}$, i.e. for the direct problem $\phi^{(\mathbf{x}_m,\omega)}_{\mathbf{x}_2} = \phi^{(\mathbf{x}_m,\omega)}_{\mathbf{x}_2+\mathbf{r}}e^{\mathrm{i}\,\varphi}$, where $\mathbf{k}$ is the wave number pointing toward the observer point $\mathbf{x}_m$. Then for a medium at rest, $\varphi = \mathbf{k}\cdot\mathbf{r} = \frac{\omega}{a_\infty}\frac{(\mathbf{x}_m-\mathbf{x}_2)}{|\mathbf{x}_m-\mathbf{x}_2|}\cdot\mathbf{r} \approx \frac{\omega}{a_\infty}\frac{\mathbf{x}_m}{|\mathbf{x}_m|}\cdot\mathbf{r}$, so that, $\phi^{(\mathbf{x}_m,\omega)}_{\mathbf{x}_2+\mathbf{r}} = \phi^{(\mathbf{x}_m,\omega)}_{\mathbf{x}_2}\exp\left(-\mathrm{i}\,\frac{\omega}{a_\infty}\frac{\mathbf{x}_m}{|\mathbf{x}_m|}\cdot\mathbf{r}\right)$, the use of the reciprocity principle $\phi^{(\mathbf{x}_m,\omega)}_{\mathbf{x}_s} = \phi^{(\mathbf{x}_s,\omega)^*}_{\mathbf{x}_m}$ then provides Eq. (B.16). It is now shown how Eq. (16) is derived considering Fraunhofer's approximation. The quantity appearing in the integrand expresses then as,

$$\mathrm{D}_{-\mathbf{u}_0,\mathbf{x}_m}\left(\phi^{\dagger(\mathbf{x}_2+\mathbf{r},\omega)}_{\mathbf{x}_m}\right) = \mathrm{D}_{-\mathbf{u}_0,\mathbf{x}_m}\left(\phi^{\dagger(\mathbf{x}_2,\omega)}_{\mathbf{x}_m}\right)\exp\left(\frac{\mathrm{i}\,\omega\;\mathbf{x}_m\cdot\mathbf{r}}{a_\infty|\mathbf{x}_m|}\right) - \phi^{\dagger(\mathbf{x}_2,\omega)}_{\mathbf{x}_m}\mathbf{u}_0\cdot\frac{\partial}{\partial\mathbf{x}_m}\left(\exp\left(\frac{\mathrm{i}\,\omega\;\mathbf{x}_m\cdot\mathbf{r}}{a_\infty|\mathbf{x}_m|}\right)\right) \tag{B.17}$$

Since $\frac{\partial}{\partial\mathbf{x}_m}\left(\frac{\mathbf{x}_m\cdot\mathbf{r}}{|\mathbf{x}_m|}\right) = \frac{|\mathbf{x}_m|^2\mathbf{r}-(\mathbf{r}\cdot\mathbf{x}_m)\mathbf{x}_m}{|\mathbf{x}_m|^3}$, the derivative along $\mathbf{u}_0$ expresses as,

$$\mathbf{u}_0\cdot\frac{\partial}{\partial\mathbf{x}_m}\left(\exp\left(\frac{\mathrm{i}\,\omega\;\mathbf{x}_m\cdot\mathbf{r}}{a_\infty|\mathbf{x}_m|}\right)\right) = \mathrm{i}\,\omega\frac{|\mathbf{x}_m|^2(\mathbf{u}_0\cdot\mathbf{r})-(\mathbf{r}\cdot\mathbf{x}_m)(\mathbf{u}_0\cdot\mathbf{x}_m)}{a_\infty|\mathbf{x}_m|^3}\exp\left(\frac{\mathrm{i}\,\omega\;\mathbf{x}_m\cdot\mathbf{r}}{a_\infty|\mathbf{x}_m|}\right) \approx \mathrm{O}\left(\frac{|\mathbf{r}|}{|\mathbf{x}_m|}\right) \tag{B.18}$$

where $|\mathbf{r}|/|\mathbf{x}_m|$ tends toward zero in Fraunhofer's approximation. Replacing this expression in the formula for S_{pp}, and by property of the Fourier transform of real valued signals, $\mathrm{D}_{-\mathbf{u}_0,\mathbf{x}_m}\left(\phi^{\dagger(\mathbf{x}_2,-\omega)}_{\mathbf{x}_m}\right) = \left[\mathrm{D}_{-\mathbf{u}_0,\mathbf{x}_m}\left(\phi^{\dagger(\mathbf{x}_2,\omega)}_{\mathbf{x}_m}\right)\right]^*$, one obtains Eq. (16). From here on $\mathbf{x}_2 \equiv \mathbf{x}_s$, and two points in the source region are defined by the first point's position $\mathbf{x}_s$ and the separation vector $\mathbf{r}$ towards the second point.

B.3. Modelling of the source correlation term R_{QQ}

Reproducing Tam and Auriault's change of variable for the integration, let $s = \tilde{\tau} - \mathbf{r}\cdot\mathbf{u}_0/u_0^2$, then it comes $\mathbf{r}-\tilde{\tau}\mathbf{u}_0 = \mathbf{r}_\perp - s\mathbf{u}_0$, where $\mathbf{r}_\perp = \mathbf{r}-(\mathbf{r}\cdot\mathbf{u}_0)\mathbf{u}_0/u_0^2$ is the projection of $\mathbf{r}$ on the hyperplane associated to $\mathbf{u}_0$ so that $\mathbf{r}_\perp\cdot\mathbf{u}_0 = 0$. The source correlation term given in Eq. (17) then becomes,

$$R_{QQ}(\mathbf{x}_s,\mathbf{r},\tilde{\tau}) = \frac{\hat{q}_s^2}{\tau_s^2}\exp\left(-\frac{|\mathbf{r}\cdot\mathbf{u}_0|}{u_0^2\tau_s} - \frac{\ln(2)|\mathbf{r}_\perp|^2}{l_s^2} - \frac{\ln(2)u_0^2s^2}{l_s^2}\right) \tag{B.19}$$

After implementing this change of variable in the noise spectrum formula, one obtains,

$$S_{pp}(\mathbf{x}_m,\omega) = \int_\Omega \mathrm{d}\mathbf{x}_s \ \frac{\hat{q}_s^2}{\tau_s^2}\left|\mathrm{D}_{-\mathbf{u}_0,\mathbf{x}_m}\left(\phi^{\dagger(\mathbf{x}_s,\omega)}_{\mathbf{x}_m}\right)\right|^2 \left[\int_{\mathbb{R}} \mathrm{d}s \ \exp\left(-\frac{\ln(2)u_0^2}{l_s^2}s^2 - \mathrm{i}\,\omega s\right)\right] \times \underbrace{\left[\int_\Omega \mathrm{d}\mathbf{r} \ \exp\left(-\frac{|\mathbf{r}\cdot\mathbf{u}_0|}{u_0^2\tau_s} - \frac{\ln(2)|\mathbf{r}_\perp|^2}{l_s^2} + \mathrm{i}\,\omega\mathbf{r}\cdot\left(\frac{\mathbf{x}_m}{a_\infty|\mathbf{x}_m|} - \frac{\mathbf{u}_0}{u_0^2}\right)\right)\right]}_{\mathcal{I}_r} \tag{B.20}$$

The integration over $\mathrm{d}s$ can now be performed making use of [71, Eq. (3.323), p.337 in 7th ed.] reprinted in Appendix A.4,

$$\int_{\mathbb{R}} \mathrm{d}s \ \exp\left(-\frac{\ln(2)u_0^2 s^2}{l_s^2} - \mathrm{i}\,\omega s\right) = \frac{l_s}{u_0}\sqrt{\frac{\pi}{\ln(2)}}\exp\left(\frac{-\omega^2 l_s^2}{4\ln(2)u_0^2}\right) \tag{B.21}$$

The integration over $\mathbf{r}$ can be performed using the split $\mathbf{r} = \mathbf{r}_\perp + \mathbf{r}_{/\!/}$ defined by the mean flow direction $\mathbf{u}_0$, where $\mathbf{r}_\perp \cdot \mathbf{u}_0 = 0$ and $\mathbf{r}_{/\!/} \times \mathbf{u}_0 = \mathbf{0}$. The volume integral $\mathcal{I}_r$ over $\mathbf{r}$ can then be split into,

$$\mathcal{I}_r = \left[\int_{\mathbb{R}} \mathrm{d}\mathbf{r}_{/\!/} \ \exp\left(-\frac{|\mathbf{r}_{/\!/}\cdot\mathbf{u}_0|}{u_0^2\tau_s} + \mathrm{i}\,\omega\mathbf{r}_{/\!/}\cdot\left(\frac{\mathbf{x}_m}{a_\infty|\mathbf{x}_m|} - \frac{\mathbf{u}_0}{u_0^2}\right)\right)\right]\left[\int_{\mathbb{R}^2} \mathrm{d}\mathbf{r}_\perp \ \exp\left(-\frac{\ln(2)|\mathbf{r}_\perp|^2}{l_s^2} + \frac{\mathrm{i}\,\omega\mathbf{r}_\perp\cdot\mathbf{x}_m}{a_\infty|\mathbf{x}_m|}\right)\right] \tag{B.22}$$

The integral over $\mathbf{r}_{/\!/}$ is evaluated using classical integral formula, given in Appendix A.4, with $\mu = \dfrac{1}{u_0\tau_s}$ and $\nu = \pm\dfrac{\omega}{u_0}\left(1 - \dfrac{\mathbf{u}_0\cdot\mathbf{x}_m}{a_\infty|\mathbf{x}_m|}\right)$,

$$\int_{\mathbb{R}} \mathrm{d}\mathbf{r}_{/\!/} \ \exp\left(-\frac{|\mathbf{r}_{/\!/}\cdot\mathbf{u}_0|}{u_0^2\tau_s} + \frac{\mathrm{i}\,\omega(\mathbf{r}_{/\!/}\cdot\mathbf{u}_0)}{u_0^2}\left(\frac{\mathbf{u}_0\cdot\mathbf{x}_m}{a_\infty|\mathbf{x}_m|} - 1\right)\right) = \frac{2u_0\tau_s}{1+\omega^2\tau_s^2\left(1 - \dfrac{\mathbf{u}_0\cdot\mathbf{x}_m}{a_\infty|\mathbf{x}_m|}\right)^2} \tag{B.23}$$

Similarly, the one running over $\mathbf{r}_\perp$ is obtaining with formula [71, Eq. (3.323), p.337 in 7th ed.] reprinted in Appendix A.4, setting $p_i = \dfrac{\sqrt{\ln(2)}}{l_s}$ and $q_i = \dfrac{\mathrm{i}\,\omega x_i}{a_\infty|\mathbf{x}_m|}$ leading to,

$$\int_{\mathbb{R}^2} \mathrm{d}\mathbf{r}_\perp \ \exp\left(-\frac{\ln(2)|\mathbf{r}_\perp|^2}{l_s^2} + \frac{\mathrm{i}\,\omega\mathbf{r}_\perp\cdot\mathbf{x}_m}{a_\infty|\mathbf{x}_m|}\right) = \frac{\pi l_s^2}{\ln(2)}\exp\left(\frac{-\omega^2 l_s^2|\mathbf{x}_{m,\perp}|^2}{4\ln(2)a_\infty^2|\mathbf{x}_m|^2}\right) \tag{B.24}$$

where $\mathbf{x}_{m,\perp} = \mathbf{x}_m - (\mathbf{x}_m\cdot\mathbf{u}_0)\mathbf{u}_0/u_0^2$. The double volume integral finally simplifies for this sound source model under Fraunhofer's condition into,

$$S_{pp}(\mathbf{x}_m,\omega) = \int_\Omega \mathrm{d}\mathbf{x}_s \ \frac{2\hat{q}_s^2 l_s^3}{\tau_s}\left(\frac{\pi}{\ln(2)}\right)^{3/2}\left|\mathrm{D}_{-\mathbf{u}_0,\mathbf{x}_m}\left(\phi^{\dagger(\mathbf{x}_2,\omega)}_{\mathbf{x}_m}\right)\right|^2 \frac{\exp\left(\dfrac{-\omega^2 l_s^2}{4\ln(2)u_0^2}\left(1 + \dfrac{u_0^2|\mathbf{x}_{m,\perp}|^2}{a_\infty^2|\mathbf{x}_m|^2}\right)\right)}{1+\omega^2\tau_s^2\left(1 - \dfrac{\mathbf{u}_0\cdot\mathbf{x}_m}{a_\infty|\mathbf{x}_m|}\right)^2} \tag{B.25}$$

Note additionally that the above expression differs from the original one by a factor of 2π, which is related to a different definition of Green's function, refer to [4, Eq. (19)], from which a $4\pi^2$ factor appears; then because of differences in the Fourier transform conventions, see [4, Eq. (25)], the present relation should be divided by 2π to comply with Tam and Auriault's relation.

B.4. Computation of $D_{-\mathbf{u}_0,\mathbf{x}_m}\left(\phi^{\dagger(\mathbf{x}_2,\omega)}_{\mathbf{x}_m}\right)$

In the previous expression the material derivative with reversed flow $\mathrm{D}_{-\mathbf{u}_0,\mathbf{x}_m}$ of $\phi^\dagger_{\mathbf{x}_m}$ needs to be evaluated. When the observer is set in a region where the fluid is at rest, the derivation is straightforward. In other cases, the knowledge of the gradient of $\phi^\dagger_{\mathbf{x}_m}$ is required along the exterior mean flow $\mathbf{u}_f$. However with the adjoint approach, Green's functions are solely known at the position $\mathbf{x}_m$. From a general point of view, the calculation of an estimate of $\mathbf{u}_0\cdot\nabla\phi^\dagger_{\mathbf{x}_m}$ is possible by additionally computing adjoint Green's function $\phi^\dagger_{\widetilde{\mathbf{x}_m}}$, where $\widetilde{\mathbf{x}_m} = \mathbf{x}_m + \varepsilon\dfrac{\mathbf{u}_f}{|\mathbf{u}_f|}$ and $\varepsilon > 0$. An estimate for the material derivative follows,

$$\begin{aligned}\mathrm{D}_{-\mathbf{u}_0,\mathbf{x}_m}\left(\phi^{\dagger(\mathbf{x}_s,\omega)}_{\mathbf{x}_m}\right) &= -\mathrm{i}\,\omega\phi^{\dagger(\mathbf{x}_s,\omega)}_{\mathbf{x}_m} - \mathbf{u}_0\cdot\nabla\phi^{\dagger(\mathbf{x}_s,\omega)}_{\mathbf{x}_m} \\ &= -\mathrm{i}\,\omega\phi^{\dagger(\mathbf{x}_s,\omega)}_{\mathbf{x}_m} - |\mathbf{u}_f|\left(\frac{\phi^{\dagger(\mathbf{x}_s,\omega)}_{\widetilde{\mathbf{x}_m}} - \phi^{\dagger(\mathbf{x}_s,\omega)}_{\mathbf{x}_m}}{\varepsilon}\right)_{\varepsilon\to 0}\end{aligned} \tag{B.26}$$

If the observer is set in the acoustic far-field this calculation can be done analytically even in presence of an ambient flow. Indeed $\phi^{\dagger(\mathbf{x}_s,\omega)}_{\widetilde{\mathbf{x}_m}}$ then differs from $\phi^{\dagger(\mathbf{x}_s,\omega)}_{\mathbf{x}_m}$ by only a phase shift φ, this is illustrated in the sketch given in Fig. B.15. The anti-causal adjoint

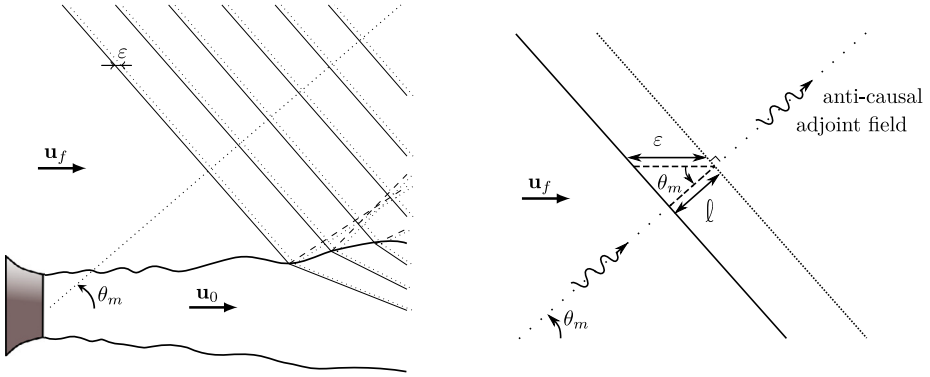

Fig. B.15. Moving from ε the adjoint source in the acoustic far-field is equivalent to add a phase shift φ.

field travels with a phase velocity $|\mathbf{v}_p| = a_\infty + |\mathbf{u}_f|\cos\theta_m$ towards the observer set in the far-field. From the anti-causality property it comes $\phi^{\dagger(\mathbf{x}_s,\omega)}_{\widetilde{\mathbf{x}_m}} / \phi^{\dagger(\mathbf{x}_s,\omega)}_{\mathbf{x}_m} = e^{\mathrm{i}\,\omega\varphi}$ with $\varphi > 0$. And the previous expression is recast into,

$$\mathrm{D}_{-\mathbf{u}_0,\mathbf{x}_m}\left(\phi^{\dagger(\mathbf{x}_s,\omega)}_{\mathbf{x}_m}\right) = \left(-\mathrm{i}\,\omega - |\mathbf{u}_f|\left[\frac{e^{\mathrm{i}\,\omega\varphi}-1}{\varepsilon}\right]_{\varepsilon\to 0}\right)\phi^{\dagger(\mathbf{x}_s,\omega)}_{\mathbf{x}_m} \tag{B.27}$$

The computation of φ with help of Fig. B.15 follows straightly, $\cos\theta_m = \ell/\varepsilon$ with $\ell = \varphi|\mathbf{v}_p|$. A Taylor expansion for small ε of the exponential function then readily gives,

$$\mathrm{D}_{-\mathbf{u}_0,\mathbf{x}_m}\left(\phi^{\dagger(\mathbf{x}_s,\omega)}_{\mathbf{x}_m}\right) = \left(-\mathrm{i}\,\omega - \mathrm{i}\,\frac{\omega|\mathbf{u}_f|\cos\theta_m}{a_\infty + |\mathbf{u}_f|\cos\theta_m}\right)\phi^{\dagger(\mathbf{x}_s,\omega)}_{\mathbf{x}_m} \tag{B.28}$$

Since the previous expression depends on the adjoint source location only by its polar angle θ_m, by defining $\phi^{\dagger(\mathbf{x}_s,\omega)}_{\mathbf{x}_m} \to \phi^{\dagger(\mathbf{x}_s,\omega)}_{\theta_m}$, a far-field expression for Tam and Auriault's mixing noise formula is obtained,

$$S_{pp}(\theta_m,\omega) = \int_\Omega \mathrm{d}\mathbf{x}_s\ \frac{2\omega^2\hat{q}_s^2 l_s^3}{\tau_s}\left(\frac{\pi}{\ln(2)}\right)^{3/2}\left|\phi^{\dagger(\mathbf{x}_s,\omega)}_{\theta_m}\right|^2\left(1+\frac{M_f\cos\theta_m}{1+M_f\cos\theta_m}\right)^2\frac{\exp\left(\dfrac{-\omega^2 l_s^2}{4\ln(2)u_0^2}\left(1+M_\infty^2\sin^2\theta_m\right)\right)}{1+\omega^2\tau_s^2\left(1-M_\infty\cos\theta_m\right)^2} \tag{B.29}$$

where $M_\infty = u_0/a_\infty$ and $M_f = |\mathbf{u}_f|/a_\infty$. It is fairly straightforward to include in these derivations an azimuthal dependency on the microphone position ψ_m as well.

Appendix C. Free field analytical solution to Pierce's equation

In Sections 2.2.3 and 2.2.5, the squared absolute value of adjoint Green's function solution of Pierce's equation $|\phi^\dagger_{\mathbf{x}_m}|^2$ and the squared absolute value of its material derivative $|\mathrm{D}_{-\mathbf{u}_0,\mathbf{x}_m}(\phi^\dagger_{\mathbf{x}_m})|^2$ are involved in the computation of the acoustic spectral density S_{pp}. Free field adjoint Green's function for a medium with an uniform flow are derived here to the sake of validation. In a first approximation, only the movement of the surrounding medium is considered to model the acoustic propagation, and Pierce's equation reduces to the convected wave equation,

$$(-\mathrm{i}\,\omega + \mathbf{u}_0\cdot\nabla)^2\phi^\dagger_{\mathbf{x}_m} - a_0^2\Delta\phi^\dagger_{\mathbf{x}_m} = \delta_{\mathbf{x}_m} \tag{C.1}$$

where $\delta_{\mathbf{x}_m}$ is an impulsive source set at the observer position. The boundary conditions of the adjoint problem are such as the solution is anti-causal, and the adjoint solution to the free field propagation problem expresses as [15],

$$\phi^{\dagger(\mathbf{x})}_{\mathbf{x}_m} = \exp\left(-\mathrm{i}\,\frac{\omega}{a_0}\frac{\mathbf{M}_0\cdot(\mathbf{x}-\mathbf{x}_m)}{1-M_0^2}\right)\frac{\exp\left(-\mathrm{i}\,\dfrac{\omega}{a_0}\dfrac{r_{\mathbf{x}_m}}{1-M_0^2}\right)}{4\pi a_0^2 r_{\mathbf{x}_m}} \tag{C.2}$$

where $r_{\mathbf{x}_m} = \sqrt{(1-M_0^2)|\mathbf{x}-\mathbf{x}_m|^2 + (\mathbf{M}_0\cdot(\mathbf{x}-\mathbf{x}_m))^2}$, and $\mathbf{M}_0 = \mathbf{u}_0/a_0$ is the vectorial Mach number. It is worth remembering that this solution is such as the reciprocity principle is fulfilled,

$$\phi^{\dagger(\mathbf{x})}_{\mathbf{x}_m} = \phi^{(\mathbf{x}_m)^*}_{\mathbf{x}} \tag{C.3}$$

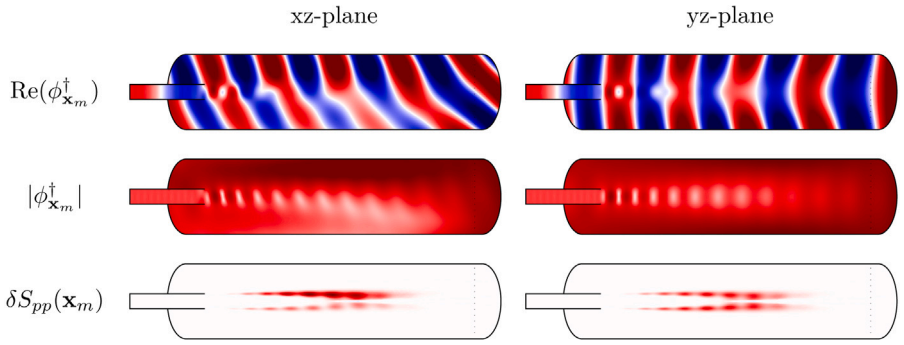

Fig. D.16. Real part and absolute part of adjoint Green's function $\phi^{\dagger}_{\mathbf{x}_m}$ for an observer at $\theta_m = 30°$ and St = 0.3. The resulting modulation of the integrand $\delta S_{pp}(\mathbf{x}_m)$ is depicted. $\mathrm{Re}(\phi^{\dagger}_{\mathbf{x}_m}) \in [-3, 3] \times 10^{-6}$ Pa·s and $|\phi^{\dagger}_{\mathbf{x}_m}| \in [0, 4] \times 10^{-6}$ Pa·s.

Then by choosing the axis in such a way that the flow is oriented along the first direction, the material derivative $\mathrm{D}_{-\mathbf{u}_0,\mathbf{x}_m}\left(\phi^{\dagger}_{\mathbf{x}_m}\right)$, expresses as,

$$\mathrm{D}_{-\mathbf{u}_0,\mathbf{x}_m}\left(\phi^{\dagger(\mathbf{x})}_{\mathbf{x}_m}\right) = -\mathrm{i}\,\omega\phi^{\dagger(\mathbf{x})}_{\mathbf{x}_m} - u_{0,1}\frac{\partial\phi^{\dagger(\mathbf{x})}_{\mathbf{x}_m}}{\partial x_1} = \left(-\mathrm{i}\,\omega + \mathrm{i}\,\omega\frac{M_0}{1-M_0^2}\left(M_0 + \frac{\partial r_{\mathbf{x}_m}}{\partial x_1}\right) + \frac{u_{0,1}}{r_{\mathbf{x}_m}}\frac{\partial r_{\mathbf{x}_m}}{\partial x_1}\right)\phi^{\dagger(\mathbf{x})}_{\mathbf{x}_m} \tag{C.4}$$

where $\partial r_{\mathbf{x}_m}/\partial x_1 = (x_1 - x_{m,1})/r_{\mathbf{x}_m}$, $\mathbf{x} = (x_1, x_2, x_3)^T$, $\mathbf{x}_m = (x_{m,1}, x_{m,2}, x_{m,3})^T$ and $\mathbf{u}_0 = (u_{0,1}, u_{0,2}, u_{0,3})^T$. A $(2\pi)^2$ difference with respect to the analytical solution derived in [30, Eqs. (49)–(50)] is noted. Remark other analytically known adjoint Green's function with a wider range of applicability could be considered [16,17].

Appendix D. Adjoint maps at $\theta_m = 30°$ and $\theta_m = 150°$

Maps of adjoint Green's functions for Strouhal numbers St = 0.3 and St = 0.9 have been reported in Section 4 for an observer located perpendicular to the jet axis in the acoustic far field. Corresponding cartography are displayed here for upstream and downstream observer positions forming shallow angles with respect to the jet axis. Adjoint Green's functions are shown for an observer at $\theta_m = 30°$ in Figs. D.16 and D.17 and for an observer located at $\theta_m = 150°$ in Figs. D.18 and D.19. Results corresponding to Strouhal numbers St = 0.3 and St = 0.9 are presented respectively.

Compared to the computations performed at $\theta_m = 90°$ and shown in Figs. 7 and 8, the presence of the jet flow causes stronger variations in the adjoint fields computed for these shallow observer angles. The fields obtained for upstream and downstream observers are however substantially different. At $\theta_m = 30°$ the jet flow causes a significant reflection of the adjoint field in the form of a horseshoe, creating a shielding in the area masked by the jet. This is most easily seen in the absolute value of adjoint Green's function presented in Fig. D.17. The acoustic reflection observed at this angle lead to low amplitudes of adjoint Green's functions in the jet potential core. At $\theta_m = 150°$ the shielding does not happen, and the levels of the adjoint fields in the region masked by the jet flow are comparable with the area directly visible from the observer location. Maximum amplitudes of adjoint Green's functions are found, this time, in the jet potential core and in the duct. As for adjoint fields calculated for an observer at $\theta_m = 90°$, the adjoint fields present modal structures in the jet plume. Their amplitudes at $\theta_m = 150°$ are however much higher.

The complete integrand of Tam and Auriault's mixing noise formula are presented for these two observer angles and two Strouhal numbers. At $\theta_m = 30°$, the shear layer region directly visible from the observer location has the largest contribution. This area is the main one selected by the squared absolute value of adjoint Green's functions. At $\theta_m = 150°$, modulation of the visible part as well as modulation of the hidden part of the shear layer contribute to the sound pressure level computed. For this upstream located observer, the shear layer part masked by the jet flow is seen to contribute the most significantly.

Appendix E. Sensitivity analysis for adjoint Green's functions computed at $\theta_m = 150°$

In Section 5.1, a base flow representative of the jet averaged flow profile (a), a simplified cylindrical vortex sheet model (c), along with a hybrid combination of the two that includes the duct geometry and a downstream smoothed truncation of the jet flow (c), have been considered. Configurations (a) and (c) model the duct as semi-infinite by absorbing the acoustic energy that enters into it by means of PML. The frequency of the tones predicted did not significantly vary for these various cases. In Section 5.2, the effect of the acoustic reflection in the duct has been investigated by considering a total reflection of the acoustic penetrating in the conduit. This last configuration, denoted (a-HW) in what follows, considers identical flow and pipe length as in case (a) but assumes a total reflection in the pipe. Compared to cases (a), (b) and (c), a tangible modification of the tone signature has been observed in this configuration. In all these cases the sound source model is unchanged, only adjoint Green's functions differ. This section compares visualisations in the xz-plane of the latter quantity to gain a broader understanding of the generation process of upstream travelling guided jet modes.

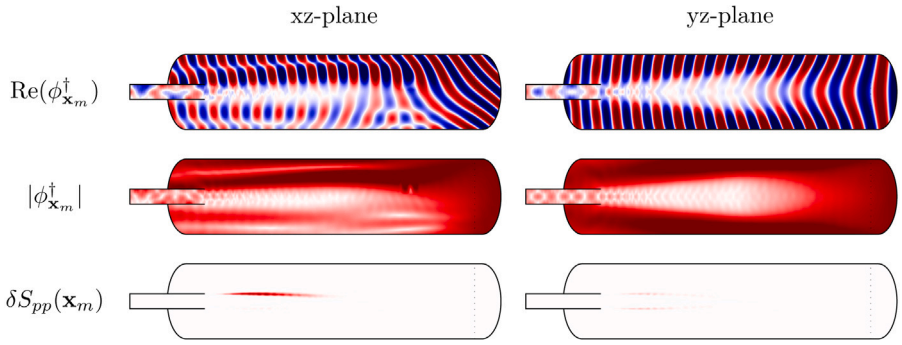

Fig. D.17. Real part and absolute part of adjoint Green's function $\phi^{\dagger}_{\mathbf{x}_m}$ for an observer at $\theta_m = 30°$ and St = 0.9. The resulting modulation of the integrand $\delta S_{pp}(\mathbf{x}_m)$ is depicted. $\mathrm{Re}(\phi^{\dagger}_{\mathbf{x}_m}) \in [-3, 3] \times 10^{-6}$ Pa·s and $|\phi^{\dagger}_{\mathbf{x}_m}| \in [0, 4] \times 10^{-6}$ Pa·s.

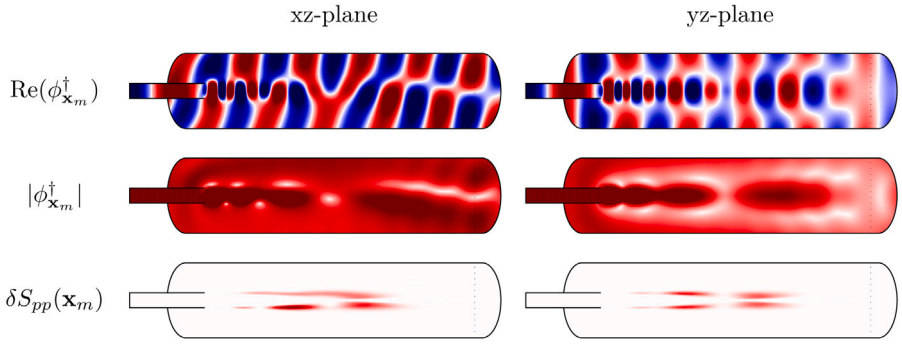

Fig. D.18. Real part and absolute part of adjoint Green's function $\phi^{\dagger}_{\mathbf{x}_m}$ for an observer at $\theta_m = 150°$ and St = 0.3. The resulting modulation of the integrand $\delta S_{pp}(\mathbf{x}_m)$ is depicted. $\mathrm{Re}(\phi^{\dagger}_{\mathbf{x}_m}) \in [-3, 3] \times 10^{-6}$ Pa·s and $|\phi^{\dagger}_{\mathbf{x}_m}| \in [0, 4] \times 10^{-6}$ Pa·s.

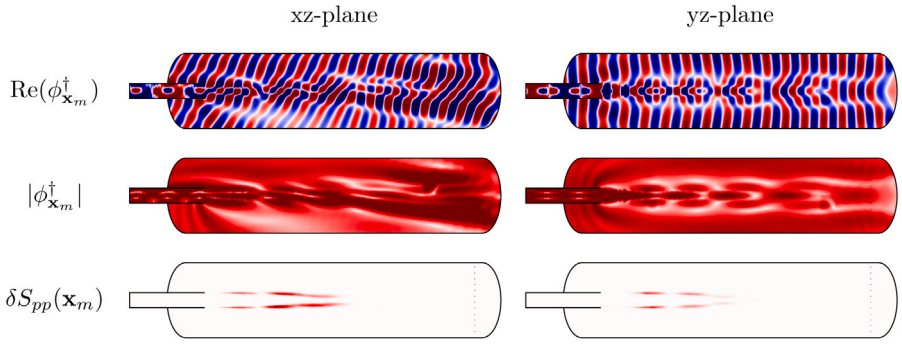

Fig. D.19. Real part and absolute part of adjoint Green's function $\phi^{\dagger}_{\mathbf{x}_m}$ for an observer at $\theta_m = 150°$ and St = 0.9. The resulting modulation of the integrand $\delta S_{pp}(\mathbf{x}_m)$ is depicted. $\mathrm{Re}(\phi^{\dagger}_{\mathbf{x}_m}) \in [-3, 3] \times 10^{-6}$ Pa·s and $|\phi^{\dagger}_{\mathbf{x}_m}| \in [0, 4] \times 10^{-6}$ Pa·s.

Absolute value of adjoint Green's functions for the cases studied in Section 5 are shown in Fig. E.20 for Strouhal numbers St = 0.27, that corresponds to the first tone, and St = 0.34, that is associated with the minima between the first and second peak. The noise level in Tam and Auriault's model is obtained from the scalar product of the absolute value of adjoint Green's functions and the sound source model, thus only the region of adjoint Green's function for which the sound source is non-zero are meaningful. In these regions, for the first peak at St = 0.27, adjoint fields computed for identical base flows are identical, i.e. the field in Fig. E.20(a) resembles to that in Fig. E.20(a - HW), and that in Fig. E.20(b) resembles to that in Fig. E.20(c). These similarities are retrieved in the acoustic predictions presented in Fig. 11 and in Fig. 12(a). The acoustic energy in the duct is not directly correlated with the in-duct boundary condition, and the effect of nozzle impedance is not recognisable at the Strouhal number of the tone. At Strouhal number St = 0.34, that is for the minima between the first and the second tone, a 3 dB difference in the noise spectra was observed between the case that model acoustic reflection in the duct (a-HW), and the configuration that does not (a). Comparing the structure of the adjoint fields of the second column in Fig. E.20, solutions for case (b) and case (c) are again alike in shape and amplitude.

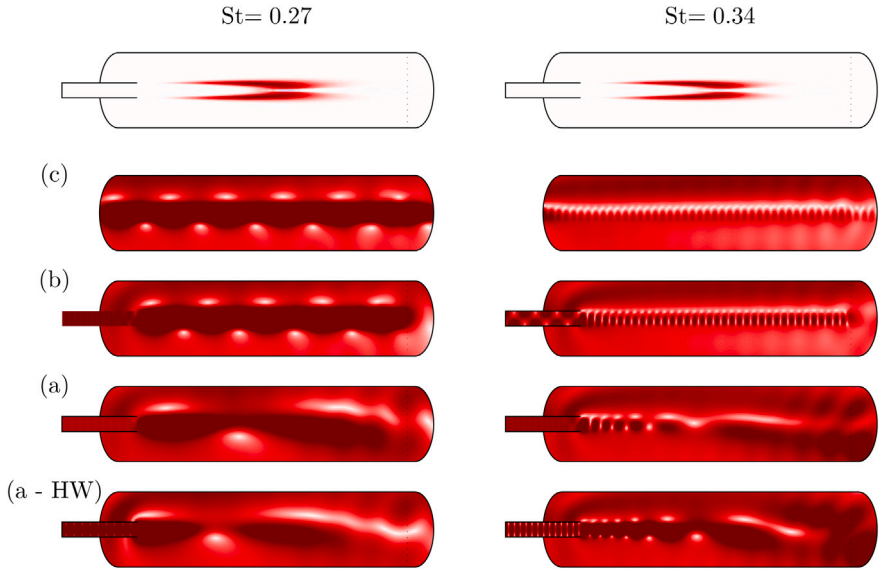

Fig. E.20. Tam and Auriault's mixing noise source model, and corresponding adjoint Green's functions $|\phi^{\dagger}_{\mathbf{x}_m}|$ in the xz-plane for St = 0.27 and St = 0.34 computed for an observer set at $\theta_m = 150°$. The modelled sound source is represented in the first row, it corresponds to the complete integrand of Eq. (18) leaving aside the squared material derivative of adjoint Green's function. The three central rows present the solution obtained for the configuration of Fig. 10, the last row shows the result obtained for a case identical to case (a) but with a permeable hard-wall boundary condition to model in-duct reflections. $|\phi^{\dagger}_{\mathbf{x}_m}| \in [0, 4] \times 10^{-6}$ Pa·s.

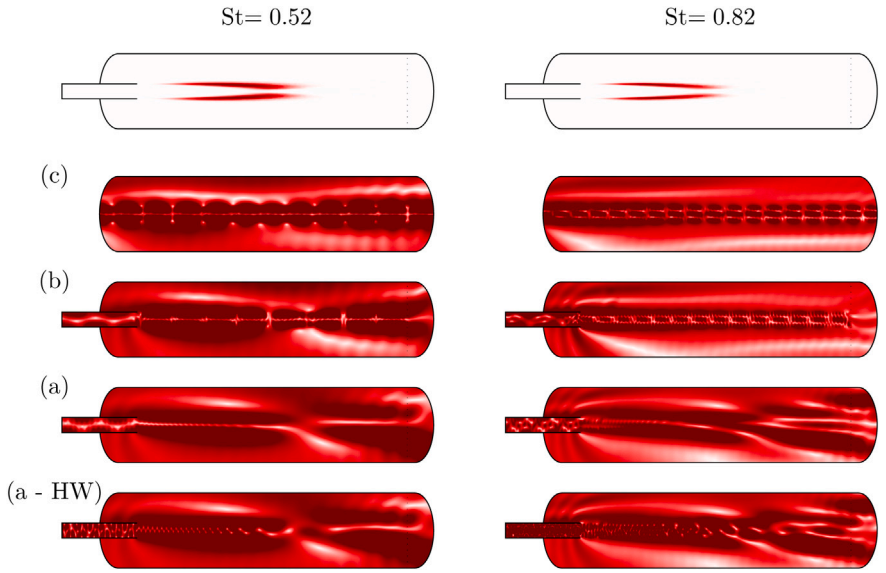

Fig. E.21. Tam and Auriault's mixing noise source model, and corresponding adjoint Green's functions $|\phi^{\dagger}_{\mathbf{x}_m}|$ in the xz-plane for St = 0.52 and St = 0.82 computed for an observer set at $\theta_m = 150°$. The modelled sound source is represented in the first row, it corresponds to the complete integrand of Eq. (18) leaving aside the squared material derivative of adjoint Green's function. The three central rows present the solution obtained for the configuration of Fig. 10, the last row shows the result obtained for a case identical to case (a) but with a permeable hard-wall boundary condition to model in-duct reflections. $|\phi^{\dagger}_{\mathbf{x}_m}| \in [0, 4] \times 10^{-6}$ Pa·s.

The case (a) and the case (a - HW) present similar structure of adjoint fields, but their amplitudes are significantly different and account for the additional 3 dB predicted.

Structure of adjoint fields tailored to the four cases studied are presented in Fig. E.21 for Strouhal numbers corresponding to the second and the third tone computed, that is for St = 0.52 and St = 0.82. The global structure of adjoint Green's functions for cases assuming a flow model with infinitely thin shear layer differ noticeably from fields considering a realistic base flow. Regular patterns in the streamwise direction are visible for the adjoint fields that consider the plug flow model which are absent from the

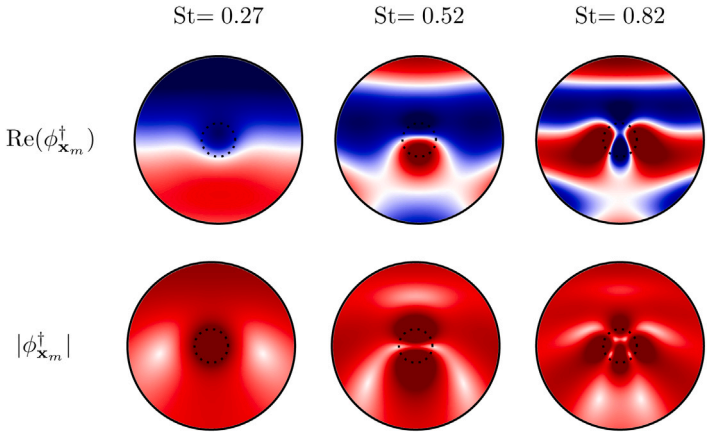

Fig. E.22. Real part and absolute part of adjoint Green's function $\phi^{\dagger}_{\mathbf{x}_m}$ computed for the case (a) and an observer at $\theta_m = 150°$. The Strouhal numbers corresponding to the first three tones are considered, extracts at $z/D_J = 5.0$ downstream of the duct exhaust are presented. $\mathrm{Re}(\phi^{\dagger}_{\mathbf{x}_m}) \in [-3, 3] \times 10^{-6}$ Pa·s and $|\phi^{\dagger}_{\mathbf{x}_m}| \in [0, 4] \times 10^{-6}$ Pa·s.

more realistic flow model. However, in the region were the sound source is significant, different tailored adjoint Green's functions are fairly comparable.

The azimuthal and radial structure of the modes in the jet for the Strouhal numbers of the first three tones are presented in Fig. E.22 for the case (a). Real part and absolute part of adjoint Green's functions extracted at $z/D_J = 5.0$ downstream of the duct are shown. The duct section is marked with a dotted circle. Tam and Ahuja [66] gave the (n_θ, n_r) eigenfunction distribution of the neutral wave modes, where n_θ corresponds to the azimuthal mode order and n_r is the radial order. Looking at the real part of the structure presented in Fig. E.22, a (0,1) mode is obtained for the first tone, a (1,1) mode for the second and a (2,1) mode for the third tone. Remarkably, the structure of these adjoint fields comply with the physical ones [48]. The contributing part of the jet can be deduced from the absolute value of adjoint Green's functions. At this axial location, it appears for the third tone, that the major contribution of the shear layer originates from the area masked by the jet.

References

[1] ECAC, Doc 29, 4th Ed. "Report on Standard Method of Computing Noise Contours around Civil Airports", Volume 1: Applications Guide, Technical report, DGCA/147, 2016.
[2] M.J. Lighthill, On sound generated aerodynamically I. General theory, in: Proc. R. Soc. Lond. A, Vol. 1107, The Royal Society London, 1952, pp. 564–587.
[3] H.S. Ribner, Aerodynamic Sound from Fluid Dilitations. A Theory of the Sound from Jets and Other Flows, Technical report, UTIA Report N^o 86, AFOSR TN 3430, University of Toronto, Institute of aerophysics, 1962.
[4] C.K.W. Tam, L. Auriault, Jet mixing noise from fine-scale turbulence, AIAA J. 37 (2) (1999) 145–153.
[5] H.S. Ribner, Quadrupole correlations governing the pattern of jet noise, J. Fluid Mech. 38 (1) (1969) 1–24.
[6] C. Bailly, P. Lafon, S.M. Candel, Subsonic and supersonic jet noise predictions from statistical source models, AIAA J. 35 (11) (1997) 1688–1696.
[7] A. Khavaran, J. Bridges, Modelling of fine-scale turbulence mixing noise, J. Sound Vib. 279 (3–5) (2005) 1131–1154.
[8] M.E. Goldstein, B. Rosenbaum, Effect of anisotropic turbulence on aerodynamic noise, J. Acoust. Soc. Am. 54 (3) (1973) 630–645.
[9] M.Z. Afsar, Insight into the two-source structure of the jet noise spectrum using a generalized shell model of turbulence, Eur. J. Mech. B Fluids 31 (2012) 129–139.
[10] M.Z. Afsar, V. Gryazev, A. Markesteijn, S.A. Karabasov, Effect of tensor representations for high-order turbulence correlations in complex axi-symmetric flow fields, in: AIAA Aviation 2021 Forum, AIAA Paper 2021-2280, Virtual envent, 2021, p. 2280.
[11] G.M. Lilley, H.E. Plumblee, W.C. Strahle, S.Y. Ruo, P.E. Doak, The Generation and Radiation of Supersonic Jet Noise. Volume IV. Theory of Turbulence Generated Jet Noise, Noise Radiation from Upstream Sources, and Combustion Noise, Technical report, Lockheed-Georgia Co. Marietta, 1972.
[12] W. Möhring, A well posed acoustic analogy based on a moving acoustic medium, in: Aeroacoustic Workshop SWING, Dresden, 1999.
[13] M.E. Goldstein, A generalized acoustic analogy, J. Fluid Mech. 488 (2003) 315–333.
[14] J.L. Lagrange, Nouvelles recherches sur la nature et la propagation du son, Oeuvres 1 (1761) 151–332.
[15] É. Spieser, C. Bailly, Sound propagation using an adjoint-based method, J. Fluid Mech. 900 (2020) A5.
[16] A.P. Dowling, J.E. Ffowcs Williams, M.E. Goldstein, Sound production in a moving stream, Philos. Trans. R. Soc. A 288 (1353) (1978) 321–349.
[17] C.K.W. Tam, L. Auriault, Mean flow refraction effects on sound radiated from localized source in a jet, J. Fluid Mech. 370 (1998) 149–174.
[18] M.E. Goldstein, S.J. Leib, The aeroacoustics of slowly diverging supersonic jets, J. Fluid Mech. 600 (2008) 291–337.
[19] S.J. Leib, M.E. Goldstein, Hybrid source model for predicting high-speed jet noise, AIAA J. 49 (7) (2011) 1324–1335.
[20] M.E. Goldstein, S.J. Leib, Azimuthal source noncompactness and mode coupling in sound radiation from high-speed axisymmetric jets, AIAA J. 56 (10) (2018) 3915–3925.
[21] N. Raizada, P.J. Morris, Prediction of noise from high speed subsonic jets using an acoustic analogy, in: 12th AIAA/CEAS Aeroacoustics Conference, AIAA Paper 2006-2596, Cambridge, Massachusetts, 2006.
[22] A. Bassetti, J.W. Nichols, Analysis of LES for source modeling in jet noise, in: 20th AIAA/CEAS Aeroacoustics Conference, AIAA Paper 2014-2905, Atlanta, Georgia, 2014.
[23] N.K. Depuru Mohan, A.P. Dowling, S.A. Karabasov, H. Xia, O. Graham, T.P. Hynes, P.G. Tucker, Acoustic sources and far-field noise of chevron and round jets, AIAA J. 53 (9) (2015) 2421–2436.

[24] S.J. Leib, D. Ingraham, J.E. Bridges, Evaluating source terms of the generalized acoustic analogy using the jet engine noise reduction (JENRE) code, in: 55th AIAA Aerospace Sciences Meeting, AIAA Paper 2017-0459, Grapevine, Texas, 2017.
[25] C. Bogey, C. Bailly, An analysis of the correlations between the turbulent flow and the sound pressure fields of subsonic jets, J. Fluid Mech. 583 (2007) 71–97.
[26] A. Towne, G.A. Brès, S.K. Lele, A statistical jet-noise model based on the resolvent framework, in: 23rd AIAA/CEAS Aeroacoustics Conference, AIAA Paper 2017-3706, Denver, Colorado, 2017.
[27] A. Adam, D. Papamoschou, C. Bogey, Imprint of vortical structures on the near-field pressure of a turbulent jet, AIAA J. 60 (3) (2022).
[28] S.A. Karabasov, T.P. Hynes, Adjoint linearised Euler solver in the frequency domain for jet noise modelling, in: 12th AIAA/CEAS Aeroacoustics Conference, AIAA Paper 2006-2673, Cambridge, Massachusetts, 2006.
[29] V.A. Semiletov, S.A. Karabasov, A 3D frequency-domain linearised Euler solver based on the Goldstein acoustic analogy equations for the study of non-uniform meanflow propagation effects, in: 19th AIAA/CEAS Aeroacoustics Conference, AIAA Paper 2013-2019, Berlin, 2013.
[30] P.J. Morris, F. Farassat, Acoustic analogy and alternative theories for jet noise prediction, AIAA J. 40 (4) (2002) 671–680.
[31] M.E. Goldstein, Ninety-degree acoustic spectrum of a high speed air jet, AIAA J. 43 (1) (2005) 96–102.
[32] M.Z. Afsar, Solution of the parallel shear layer Green's function using conservation equations, Int. J. Aeroacoust. 8 (6) (2009) 585–602.
[33] M.E. Goldstein, A. Sescu, M.Z. Afsar, Effect of non-parallel mean flow on the Green's function for predicting the low-frequency sound from turbulent air jets, J. Fluid Mech. 695 (2012) 199–234.
[34] M.Z. Afsar, A. Sescu, S.J. Leib, Modelling and prediction of the peak-radiated sound in subsonic axisymmetric air jets using acoustic analogy-based asymptotic analysis, Philos. Trans. R. Soc. A 377 (2159) (2019) 20190073.
[35] M.Z. Afsar, A. Sescu, V. Sassanis, Effect of non-parallel mean flow on the acoustic spectrum of heated supersonic jets: Explanation of "jet quietening", Phys. Fluids 31 (10) (2019) 105107.
[36] M.Z. Afsar, A. Sescu, V. Gryazev, A.P. Markesteijn, S.A. Karabasov, Analysis of the non-parallel flow-based Green's function in the acoustic analogy for complex axisymmetric jets, in: 26th AIAA/CEAS Aeroacoustics Conference, AIAA Paper 2020-2507, Virtual envent, 2020.
[37] C.K.W. Tam, N.N. Pastouchenko, K. Viswanathan, Continuation of near-acoustic fields of jets to the far field. Part I: Theory, in: 16th AIAA/CEAS Aeroacoustics Conference, AIAA Paper 2010-3728, Stockholm, 2010.
[38] C.K.W. Tam, K. Viswanathan, N.N. Pastouchenko, B. Tam, Continuation of near-acoustic fields of jets to the far field. Part II: Experimental validation and noise source characteristics, in: 16th AIAA/CEAS Aeroacoustics Conference, AIAA Paper 2010-3729, Stockholm, 2010.
[39] C.K.W. Tam, M. Golebiowski, J. Seiner, On the two components of turbulent mixing noise from supersonic jets, in: 2nd AIAA/CEAS Aeroacoustics Conference, AIAA Paper 1996-1716, State College, Pennsylvania, 1996.
[40] C. Bogey, C. Bailly, D. Juvé, Computation of flow noise using source terms in linearized Euler's equations, AIAA J. 40 (2) (2002) 235–243.
[41] C. Bailly, C. Bogey, S. Candel, Modelling of sound generation by turbulent reacting flows, Int. J. Aeroacoust. 9 (4–5) (2010) 461–489.
[42] A.D. Pierce, Wave equation for sound in fluids with unsteady inhomogeneous flow, J. Acoust. Soc. Am. 87 (6) (1990) 2292–2299.
[43] M.S. Howe, Acoustics of Fluid-Structure Interactions, Cambridge University Press, 1998.
[44] C. Bogey, Grid sensitivity of flow field and noise of high-Reynolds-number jets computed by large-eddy simulation, Int. J. Aeroacoust. 17 (4–5) (2018) 399–424.
[45] C. Bogey, O. Marsden, C. Bailly, Large-eddy simulation of the flow and acoustic fields of a Reynolds number 10^5 subsonic jet with tripped exit boundary layers, Phys. Fluids 23 (3) (2011) 035104.
[46] C. Bogey, R. Sabatini, Effects of nozzle-exit boundary-layer profile on the initial shear-layer instability, flow field and noise of subsonic jets, J. Fluid Mech. 876 (2019) 288–325.
[47] C. Bogey, A database of flow and near pressure field signals obtained for subsonic and nearly ideally expanded supersonic free jets using large-eddy simulations, 2022, https://hal.archives-ouvertes.fr/hal-03626787.
[48] C. Bogey, Acoustic tones in the near-nozzle region of jets: characteristics and variations between Mach numbers 0.5 and 2, J. Fluid Mech. 921 (2021) A3.
[49] C. Bogey, Tones in the acoustic far field of jets in the upstream direction, AIAA J. 60 (4) (2022).
[50] R.H. Self, M. Azarpeyvand, Utilization of turbulent energy transfer rate time-scale in aeroacoustics with application to heated jets, Int. J. Aeroacoust. 7 (2) (2008) 83–102.
[51] C. Bailly, G. Comte-Bellot, Turbulence, in: Experimental Fluid Mechanics, Springer, Heidelberg, 2015.
[52] V. Fleury, C. Bailly, E. Jondeau, M. Michard, D. Juvé, Space-time correlations in two subsonic jets using dual particle image velocimetry measurements, AIAA J. 46 (10) (2008) 2498–2509.
[53] M.Z. Afsar, Asymptotic properties of the overall sound pressure level of subsonic jet flows using isotropy as a paradigm, J. Fluid Mech. 664 (2010) 510–539.
[54] P. Pineau, C. Bogey, Numerical investigation of wave steepening and shock coalescence near a cold Mach 3 jet, J. Acoust. Soc. Am. 149 (1) (2021) 357–370.
[55] C. Bogey, S. Barré, V. Fleury, C. Bailly, D. Juvé, Experimental study of the spectral properties of near-field and far-field jet noise, Int. J. Aeroacoust. 6 (2) (2007) 73–92.
[56] A.V.G. Cavalieri, P. Jordan, W.R. Wolf, Y. Gervais, Scattering of wavepackets by a flat plate in the vicinity of a turbulent jet, J. Sound Vib. 333 (24) (2014) 6516–6531.
[57] S. Piantanida, V. Jaunet, J. Huber, W.R. Wolf, P. Jordan, A.V.G. Cavalieri, Scattering of turbulent-jet wavepackets by a swept trailing edge, J. Acoust. Soc. Am. 140 (6) (2016) 4350–4359.
[58] C. Bogey, Generation of excess noise by jets with highly disturbed laminar boundary-layer profiles, AIAA J. 59 (2) (2021) 569–579.
[59] A.Z. Karon, K.K. Ahuja, Role of nozzle-exit boundary layer in producing jet noise, Int. J. Aeroacoust. (1–28) (2022).
[60] K.B.M.Q. Zaman, Effect of initial boundary-layer state on subsonic jet noise, AIAA J. 50 (8) (2012) 1784–1795.
[61] É. Spieser, C. Legendre, C. Bailly, Solution of Pierce's equation for Tam & Auriault's mixing noise model, in: AIAA Aviation 2021 Forum, AIAA Paper 2021-2238, Virtual envent, 2021, p. 2238.
[62] A. Ruggiero, R. D'Amato, S. Affatato, Comparison of meshing strategies in THR finite element modelling, Materials 12 (14) (2019) 2332.
[63] B. Van Antwerpen, Y. Detandt, D. Copiello, E. Rosseel, E. Gaudry, Performance improvements and new solution strategies of Actran TM for nacelle simulations, in: 20th AIAA/CEAS Aeroacoustics Conference, AIAA Paper 2014-2315, Atlanta, Georgia, 2014.
[64] A. Towne, A.V.G. Cavalieri, P. Jordan, T. Colonius, O. Schmidt, V. Jaunet, G.A. Brès, Acoustic resonance in the potential core of subsonic jets, J. Fluid Mech. 825 (2017) 1113–1152.
[65] K.B.M.Q. Zaman, A.F. Fagan, P. Upadhyay, Pressure fluctuations due to 'trapped waves' in the initial region of compressible jets, J. Fluid Mech. 931 (2022).
[66] C.K.W. Tam, K.K. Ahuja, Theoretical model of discrete tone generation by impinging jets, J. Fluid Mech. 214 (1990) 67–87.
[67] O.T. Schmidt, A. Towne, T. Colonius, A.V.G. Cavalieri, P. Jordan, G.A. Brès, Wavepackets and trapped acoustic modes in a turbulent jet: coherent structure eduction and global stability, J. Fluid Mech. 825 (2017) 1153–1181.
[68] L. Selle, F. Nicoud, T. Poinsot, Actual impedance of nonreflecting boundary conditions: Implications for computation of resonators, AIAA J. 42 (5) (2004) 958–964.
[69] T. Emmert, P. Lafon, C. Bailly, Numerical study of self-induced transonic flow oscillations behind a sudden duct enlargement, Phys. Fluids 21 (10) (2009) 106105.
[70] U. Ingard, V.K. Singhal, Effect of flow on the acoustic resonances of an open-ended duct, J. Acoust. Soc. Am. 58 (4) (1975) 788–793.
[71] I.S. Gradshteyn, I.M. Ryzhik, Table of Integrals, Series, and Products, Academic Press, New York, 1965.